

Pervasive carbonation of peridotite to listvenite (Semail Ophiolite, Sultanate of Oman): clues from iron partitioning and chemical zoning

Thierry Decrausaz¹, Marguerite Godard¹, Manuel Menzel^{2,3}, Fleurice Parat¹, Emilien Olliot¹, Romain Lafay¹, Fabrice Barou¹

5 ¹Géosciences Montpellier, Université de Montpellier, CNRS, Montpellier, 34095, France

²Tectonics and Geodynamics, RWTH Aachen University, Aachen, D-52056, Germany

³Instituto Andaluz de Ciencias de la Tierra (IACT), CSIC-UGR, Armilla, 18100, Spain

Correspondence to: Thierry Decrausaz (thierry.decrausaz@umontpellier.fr)

10 **Abstract.** Earth's long-term cycling of carbon is regulated from mid-ocean ridges to convergent margins by mass transfers involving mantle rocks. Here we examine the conversion of peridotite into listvenite (magnesite+quartz) occurring along the basal thrust of the Semail Ophiolite (Fanja, Sultanate of Oman). At the outcrop scale, this transformation defines reaction fronts, from serpentinized peridotites, to carbonated serpentinites and listvenites. Carbonation of peridotites progressed through distinctive stages, involving the generation of carbonate and/or quartz veins concurrently to the pervasive replacement of
15 serpentinized peridotites by carbonates and quartz. The onset of pervasive carbonation reactions is characterized by the formation of Fe-rich magnesite spheroids and aggregates preserved in listvenites, in the vicinity of antitaxial Fe-rich magnesite veins.

We document the changes in reaction textures and carbonate compositions from carbonated serpentinites to listvenites, indicating destabilization of Fe-oxides. We propose that Fe-rich cores of magnesite spheroids result from the breakdown of magnetite into Fe-rich magnesite and hematite, and represent the end product of the early carbonation sequence. Pervasive
20 carbonation induces a change to oxidizing conditions as the reaction progresses. We discuss the linkages between the composition of magnesite replacing the serpentine matrix and variations of the reactive fluid composition and redox conditions, and their possible effects on the speciation of volatiles and mobility of economically-valuable metals.

1 Introduction

25 (De-)hydration and (de-)carbonation of peridotites play a major role on the long-term cycling of volatiles, incompatible and fluid-mobile elements between the surface and the deep Earth (e.g., Alt et al., 2013; Deschamps et al., 2013; Kelemen and Manning, 2015; Bouilhol et al., 2022). Carbonation of peridotites takes place in various hydrothermal systems, from seafloor to the interface between converging plates (e.g., Delacour et al., 2008; Schwarzenbach et al., 2013; Scambelluri et al., 2016; Debret et al., 2018; Noël et al., 2018), or during (sub-)surface weathering (e.g., Kelemen and Matter, 2008; Ulrich et al., 2014).

30 The high content of divalent cations (Mg, Fe, Ca) in peridotites favours CO₂ trapping by carbonate precipitation, hence potentially providing a mean to mitigate anthropogenic emissions (Seifritz, 1990; Matter and Kelemen, 2009; Power et al., 2013). Listvenites represent the most extreme products of peridotite carbonation, with the complete conversion of olivine, orthopyroxene (Opx) and clinopyroxene (Cpx) into magnesite and quartz (\pm dolomite, fuchsite) (Halls and Zhao, 1995). Listvenites and related carbonated serpentinites are found throughout many ophiolite complexes worldwide, typically at the
35 interface between mantle rocks and mafics or clastic sediments along major shear zones (e.g., Hansen et al., 2005; Beinlich et al., 2012; Aftabi and Zarrinkoub, 2013; Hinsken et al., 2017; Sofiya et al., 2017; Qiu and Zhu, 2018; Menzel et al., 2018; Boskabadi et al., 2020). Listvenite formation testifies of major mass transfers (Kelemen and Manning, 2015). Over the recent years, the possible reaction pathways and mechanisms leading to complete peridotite carbonation have been investigated (e.g. Hansen et al., 2005; Tominaga, et al., 2017; Menzel et al., 2018) but our understanding of Fe-partitioning and related changes
40 in redox conditions during these reactions remain not fully understood.

The most extended outcrops of listvenites are observed in the Semail Ophiolite in Oman (Glennie et al., 1974; Stanger, 1985; Wilde et al., 2002; Nasir et al., 2007; Falk and Kelemen, 2015; Boudier and Nicolas, 2018), and have been the focus of Hole BT1B of the Oman Drilling Project, which sampled listvenites, serpentinites and the metamorphic sole at the base of the ophiolite at Wadi Mansah (Fanja region) (Kelemen et al., 2020). The unmatched density and quality of borehole samples open
45 up unique opportunities to investigate the reaction sequence leading to pervasive replacement of serpentinitized peridotite by carbonates.

We present the results of a detailed study of the field relationships, petrology, and textures of the Fanja listvenites and adjacent serpentinitized peridotites and their mineral compositions (silicates, carbonates, oxides and sulphides). We document the reaction sequence and matrix replacement textures characterizing incipient to pervasive carbonation, and discuss the conditions
50 at which these reactions may have occurred. We also discuss the impact of carbonation on the redistribution of Fe and transition metals between oxides, sulphides, and carbonates, and linkages to fluid fluxes and redox conditions.

2 Geological setting and sampling

2.1 The Semail Ophiolite and outcropping listvenites

The Semail Ophiolite is a segment of Tethyan oceanic lithosphere obducted on the Arabian continental margin during the
55 Upper Cretaceous (e.g., Coleman, 1981; Nicolas et al., 2000) (Fig. 1a). It preserves a thick mantle section overlain by a layered oceanic crust, comprising lower layered gabbros to upper volcanics. A commonly 10–100 m thick metamorphic sole made up of slivers of mafic and sedimentary-derived material outcrops discontinuously along the base of the ophiolite (e.g., Soret et al., 2017). The ophiolite mantle is composed of moderately to highly serpentinitized harzburgites and minor dunites, with Cpx-harzburgites and lherzolites locally found toward the base of the section (Lippard et al., 1986; Godard et al., 2000; Takazawa
60 et al., 2003; Boudier et al., 2010; Hanghøj et al., 2010). A 50–200 m thick section of highly serpentinitized, mylonitized and

often amphibole-bearing Cpx-rich peridotites alternating with dunites and minor harzburgites commonly characterizes the basal transition of the ophiolite to its metamorphic sole (e.g., Khedr et al., 2013; Prigent et al., 2018). The sole records peak

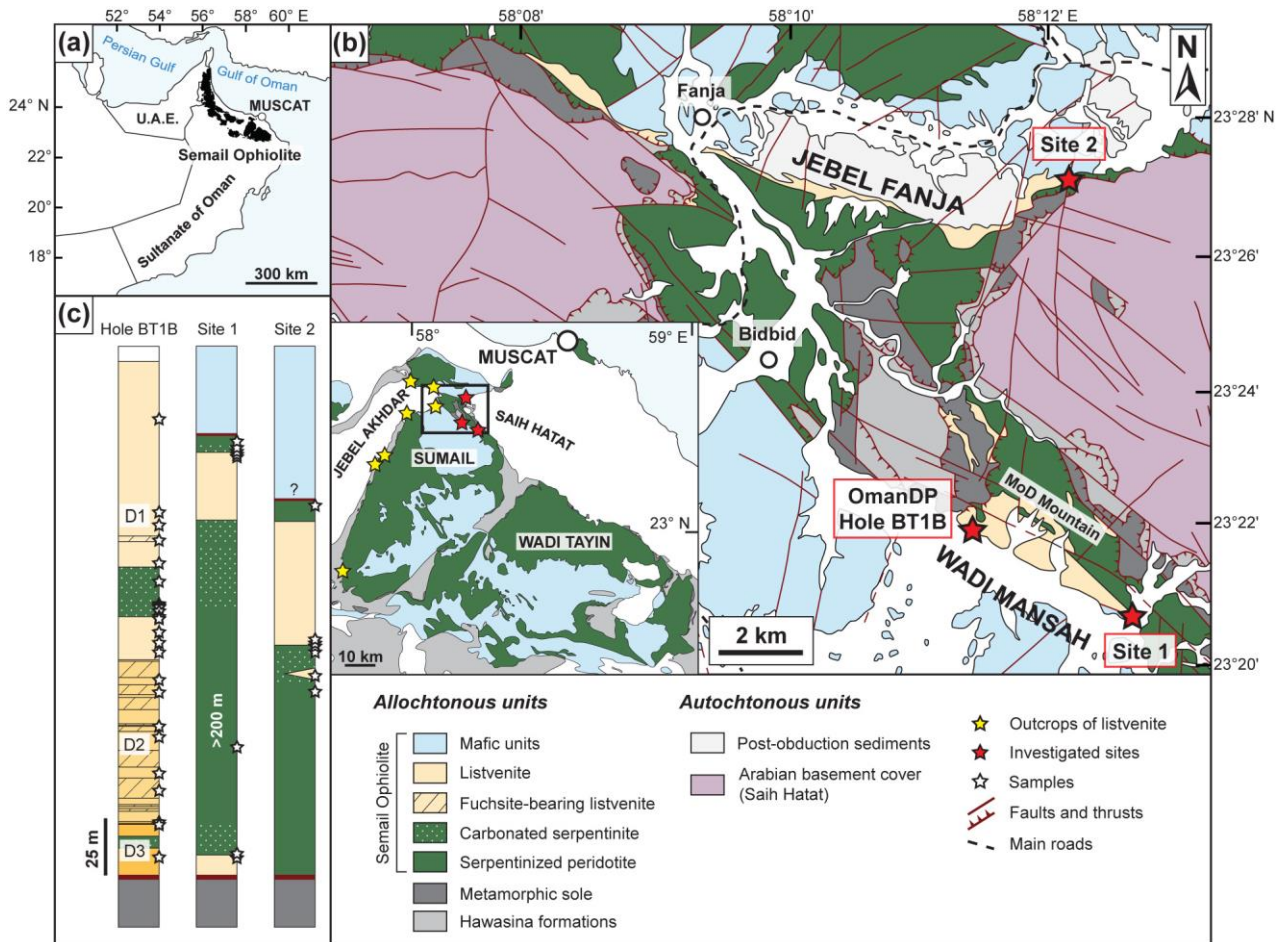


Figure 1: Listvenite outcrops in the Fanja area (Semail Ophiolite). (a) Location of the Ophiolite. (b) Geological map of the Fanja area (modified after Villey et al. (1986), Kelemen et al. (2022)), indicated by a black rectangle in the insert map (after Nicolas et al., 2000). Listvenite occurrences (yellow stars) from Nasir et al. (2007) and Boudier and Nicolas (2018), (c) Lithological columns for Hole BT1B, Sites 1 and 2. D1, D2 and D3 protolith domains after Godard et al. (2021).

metamorphism in amphibolite to granulite facies ascribed to intra-oceanic underthrusting (e.g., Boudier et al., 1988) or incipient subduction (e.g., Searle and Cox, 1999). Zircon dating indicates that the formation of the sole was in part contemporaneous to the accretion of the oceanic crust preserved by the ophiolite (96.1–95.2 Ma; Rioux et al., 2021). The ophiolite and metamorphic sole, when present, were thrust over the allochthonous Hawasina formations during convergence. The Hawasina formations comprises volcanics, pelagic and shelf sediments, witnessing the existence of a wide oceanic basin prior to obduction of the ophiolite (Bechennec et al., 1990). Ophiolite obduction and burial of autochthonous Arabian basement rocks (85–77 Ma) was followed by an extensional phase of exhumation forming the Jebel Akhdar and Saih Hatat domes (Garber et al., 2021).

Listvenites crop out discontinuously along the ophiolite basal thrust (Fig. 1b). They occur as decametric thick layers and lenses within serpentinite oriented parallel to the basal thrust, or as blocks within tectonic mélanges in shear zones (Nasir et al., 2007). This study focusses on the Fanja region, where the best exposed outcrops of listvenites are observed (Fig. 1b). The Fanja ophiolite section is relatively thin (Boudier and Nicolas, 2018) and exposes dismembered and highly faulted fragments of mantle peridotites juxtaposed with lower gabbros and slices of metamorphic sole. The listvenites are aligned along a NW–SE direction to the North and the South of ophiolite segments flanking the Jebel Akhdar and Saih Hatat domes. Fieldwork and sampling of serpentinitized peridotites, carbonated serpentinites and listvenites was carried out along transects from the metamorphic sole to the overlying gabbros at 3 sites (Fig. 1b): OmanDP Hole BT1B, exposing the largest outcrops of listvenites, Site 1 in Wadi Mansah (southern alignment of listvenites) and Site 2 in the Jebel Fanja (northern alignment of listvenites).

2.2 Sampling

2.2.1 OmanDP Hole BT1B

Hole BT1B recovered ~200 m of listvenites interlayered by two levels of carbonated serpentinites, atop of ~100 m of metamorphic rocks (Kelemen et al., 2020) (Fig. 1c). Bulk rock geochemical analyses of the mantle-derived section revealed three chemically distinct domains indicating that its protolith comprised alternating harzburgites/dunites and lherzolites as commonly observed along the ophiolite basal thrust (Godard et al., 2021) (Fig. 1c). Listvenites comprise dominantly magnesite and quartz forming the rock matrix along with minor dolomite and fuchsite, and accessory (relict) Cr-spinel, hematite and Fe-hydroxides. Fuchsite is observed only in listvenites from the lherzolic protolith domain. Listvenites and carbonated serpentinites are cut by numerous generations of different carbonate and quartz veins (Kelemen et al., 2020; Menzel et al., 2022) and cataclasites (Menzel et al., 2020). 15 listvenites, 5 fuchsite-bearing listvenites and 9 carbonated serpentinites were selected for this study.

2.2.2 Site 1 and Site 2

Site 1 is located in the south-eastern part of Wadi Mansah, ~4.5 km east from Hole BT1B (Fig. 1b, Fig. S1). The mantle section (>250 m) is composed of massive serpentinitized harzburgites and rare dunites. Listvenites are found atop the metamorphic sole to the North, or interlayering peridotites close to gabbros to the South (Fig. 1c). Lithological boundaries dip to the SSW and, except for the listvenite-peridotite interlayering, all contacts are faulted. Listvenites are stain orange-red due to weathering. The sole comprises, from top to bottom, mafic-derived rocks and metasediments. Listvenites in contact with the basal thrust form a 2–10 m thick layer below ~20 m of foliated and fractured carbonated serpentinites (Fig. S1). In the southern part, listvenites form a 10–50 m thick interval bordered by foliated and fractured carbonated serpentinites, 5–10 m from the faulted contact with foliated gabbros. Listvenites are massive and host discontinuous millimetric to centimetric quartz-carbonate veins oriented at high angle with the lithological contact. Fault contacts between listvenites, serpentinites and gabbro are highly

variable, ranging from serpentinite fault gouge to foliated serpentinite, with sharp localized faults. Close to gabbros, carbonated serpentinites host scarce gabbroic dikelets (<10 cm thick) or pods. Away from gabbros, ~25–50 m of deformed serpentinites show extensive matrix replacement by carbonates. Sampling includes 1 serpentinitized harzburgite, 4 carbonated serpentinites and 3 listvenites (Fig 1c, Table S1).

Site 2 is located in the north-eastern part of the Jebel Fanja, 9.5 km north from Hole BT1B (Fig. 1b-c, Fig. S1). This area exposes a ~150 m thick mantle section comprising serpentinitized harzburgites, interlayered by stain orange-red listvenites to the North, close to overlying gabbros. Lithological boundaries dip to the NNW. Often foliated and fractured serpentinitized harzburgites (~100 m thick) overlie the metamorphic sole. The sole comprises, from top to bottom, mafic-derived schists, with amphibolites locally along the basal thrust, atop metasediments. Listvenites are found as a ~50–75 m thick continuous planar structural level close to gabbros, draping the ridge and southern flank of the Jebel Fanja, and as plurimetric lenses within carbonated serpentinites. Listvenites are massive and crosscut by closely spaced sub-millimetric orange-red magnesite veins and by millimetric white quartz-carbonate veins, all oriented perpendicular to the contact with the underlying carbonated serpentinites (~3–20 m). Carbonated serpentinites are often foliated at the contact with listvenites and host millimetric to centimetric light orange magnesite veins, oriented at low-angle with the contact (Fig. S2). Vein density increases towards listvenites. Few millimetric red magnesite veins cut through both listvenites and carbonated serpentinites. Listvenites are overlain by serpentinitized peridotites (>20 m) cross-cut by numerous gabbroic dikes and pods at proximity with gabbros. Sampling includes 2 serpentinitized harzburgites, 3 carbonated serpentinites and 3 listvenites collected along two transects (Fig 1c, Table S1).

125 **3 Petrographic, analytical and modelling methods**

The petrography, microstructure and composition of carbonated serpentinites and listvenites were determined and mapped using optical microscopy and a CamScan CrystalProbe X500FE Scanning Electron Microscope (SEM), equipped with UltimMax 100 EDS (energy-dispersive X-ray spectroscopy) detector at the Géosciences Montpellier SEM-EBSD facility. EDS data were processed with Oxford Instruments Aztec. Further back-scattered and secondary electron images were acquired using a Zeiss Gemini SUPRA 55 field-emission scanning electron microscope (FE-SEM) at the Institute of Tectonics and Geodynamics of RWTH Aachen University. Mineral compositions of carbonates, silicates (serpentine, fuchsite), oxides and sulphides were quantified, and mapped for a subset of 25 samples, using a Cameca SX100 (Géosciences Montpellier) and a JEOL JXA-8530F HyperProbe (ISTE, University of Lausanne) Electron Probe Micro-Analyzer (EPMA). Elemental maps were quantified by coupling EDS semi-quantitative data and EPMA compositions using XMapTools 3.4.1 MatLab toolbox (Lanari et al., 2019). Trace element compositions of carbonates were measured for a subset of 12 samples by laser ablation inductively-coupled plasma mass spectrometry (LA-ICP-MS) on a ThermoScientific Element XR mass spectrometer (ISTE) and a ThermoScientific Element 2 mass spectrometer (Géosciences Montpellier). Data were processed using Glitter (Griffin

et al., 2008). Sample preparation, operating conditions, analytical and data processing protocols are reported in Text S1. Analytical errors and measurements on reference materials are provided in Tables S3 and S9.

140 Thermodynamic calculations were performed using Perple_X 6.9.1 (Connolly, 2005, 2009), in a H₂O-CO₂ saturated FeO-Fe₂O₃-MgO-SiO₂ system to constrain the stability fields of metasomatic assemblages resulting from carbonation. The calculations were performed using the TC-DS622 version of the Holland and Powell (2011) thermodynamic data base with equations of state for H₂O and CO₂ after Pitzer and Sterner (1995). Solid solution models were applied for magnesite-siderite (Holland and Powell, 1998), antigorite (Padrón-Navarta et al., 2013), and ideal solution models for talc and brucite. Hematite, 145 magnetite, and quartz were considered as pure phases.

4 Results

4.1. Rock types and mineralogy

Peridotites at Sites 1 and 2 are moderately to highly serpentinized harzburgites preserving a porphyroclastic texture (Fig. S3). Olivine appears as mesh cores rimmed by serpentine (lizardite/chrysotile) and magnetite strings. Opx shows incipient 150 pseudomorphic replacement to bastite with serpentine along fractures and cleavages. Minor Cpx occurs at the rim or close to Opx. Cr-spinel is found within the serpentine mesh or close to Opx. Rare sulphides, identified as Fe-Ni-Co-bearing by SEM-EDS (harzburgite OM20-13), are also observed in the mesh. Partially serpentinized harzburgites host rare millimetric veins composed of light yellowish serpentine on vein walls and dark greenish serpentine in the median zone.

Carbonated serpentinites preserve the serpentine hourglass and bastite textures, and related magnetite strings, along with 155 matrix-replacive carbonates (e.g., Fig. S3). Magnesite and subordinate dolomite predominate at Sites 1 and 2 and in BT1B cores. Carbonated serpentinites also contain relicts of Cr-spinel, often thinly rimmed by magnetite or ferri-chromite, and rare polydymite, a weathering product of pentlandite (serpentinite 44Z-4-0-5). Carbonated serpentinites host various generations of chrysotile veins locally replaced by carbonates, carbonate veins, and less common quartz veins (Table S2).

Listvenites have a fine-grained matrix of quartz (locally chalcedony), magnesite and subordinate dolomite (Fig. S3). Relicts 160 of variously altered Cr-spinel are preserved. Fuchsite was identified only in Hole BT1B samples. It frequently grows at the expense of Cr-spinel (e.g., listvenite 68Z-1-60-64), or is intergrown with quartz in aggregates resembling bastite (e.g., listvenite 53Z-2-72-77). Anhedral to flaky hematite (~5–20 µm) occurs within the magnesite-quartz matrix, rimming altered Cr-spinel, and replacing magnetite. Locally, hematite is in turn altered to goethite. Few BT1B core intervals contain accessory pyrite (e.g., listvenite 46Z-4-46-51), and, rarely, polydymite, chalcocite and gersdorffite (e.g., listvenite 46Z-2-19-24). Listvenites 165 host an intricate network of carbonate and (carbonate-)quartz veins (Table S2).

Sulphides are very rare in the Fanja samples, especially in listvenites. Fe-oxides and sulphides assemblages varies in the different carbonated lithologies: magnetite and rare awaruite (Beinlich et al., 2020) were observed in slightly carbonated

serpentinite, magnetite and Fe-Ni rich sulphides dominate in carbonated serpentinite, whilst hematite and rare Fe-Cu rich sulphides characterize listvenite.

170 4.2 Veins and replacive textures in the matrix

Carbonation of serpentinized peridotites is characterized by the development of carbonate-bearing veins (up to 50% of carbonated serpentinites and listvenites) and by the pervasive replacement of the host rock matrix by carbonates (Table S2). Menzel et al. (2022) document the sequence of veins (mineralogy and morphology) generated during carbonation progress at Hole BT1B. Thereafter, we summarize the different stages of veining and pervasive carbonate replacement recorded in BT1B
175 cores and in our Fanja samples, using the nomenclature of Menzel et al. (2022) for mesh and vein textures.

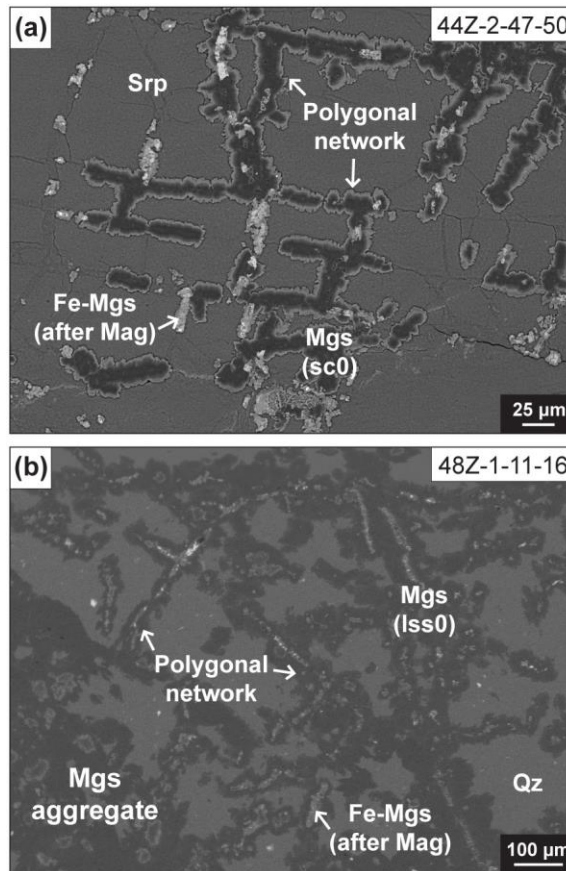


Figure 2: Back-scattered electron (BSE) images of pseudomorphic replacement textures of serpentine mesh rims by carbonates (sc0 and lss0), forming characteristic polygonal networks in (a) carbonated serpentinite 44Z-2-47-50) and (b) listvenite (48Z-1-6-11). Fe-rich magnesite (light grey) formed at the expense of magnetite. Abbreviations: Mgs: magnesite, Qz: quartz, Srp: serpentine.

180 The first stage of carbonation reactions is the replacement of serpentine mesh rims (“ss0” <20 μm, Fig. 2a) and crack-seal veins (“ss2”, 50 μm to ~2 mm; Fig. 3a) to form early carbonate veins (“sc0”) in serpentinized peridotites. The pseudomorphosed mesh rims (“lss0”) and veins (“lss2”) characterizing listvenites represent relicts of this incipient carbonation

stage; they record the complete conversion of serpentine to columnar or fibrous magnesite and quartz (Figs. 2b). These microstructures are cut by anastomosing or closely-spaced, parallel antitaxial magnesite veins (20–500 μm , Fig. 3a). Antitaxial

185 veins are the dominant vein type in carbonated serpentinites (“sc2”) and listvenites (“lc1”). They commonly display blocky to fibrous textures, typically showing crystal growth from a well-defined median zone toward vein walls, with euhedral crystal terminations. The median zone is composed of magnesite or, occasionally, dolomite, with Fe-oxides or hydroxides in the vicinity of the median line. The development of irregular-shaped, cross-fibre to blocky magnesite veins (50–300 μm , “sc3” in

190 serpentinitized peridotites and “lc2” in listvenites) ends the first steps of carbonation reactions, before pervasive matrix replacement by carbonate and quartz in listvenites. The last stage of veining generates syntaxial carbonate- and quartz-bearing veins cutting both carbonated serpentinites and listvenites (see Text S1-2 for further details).

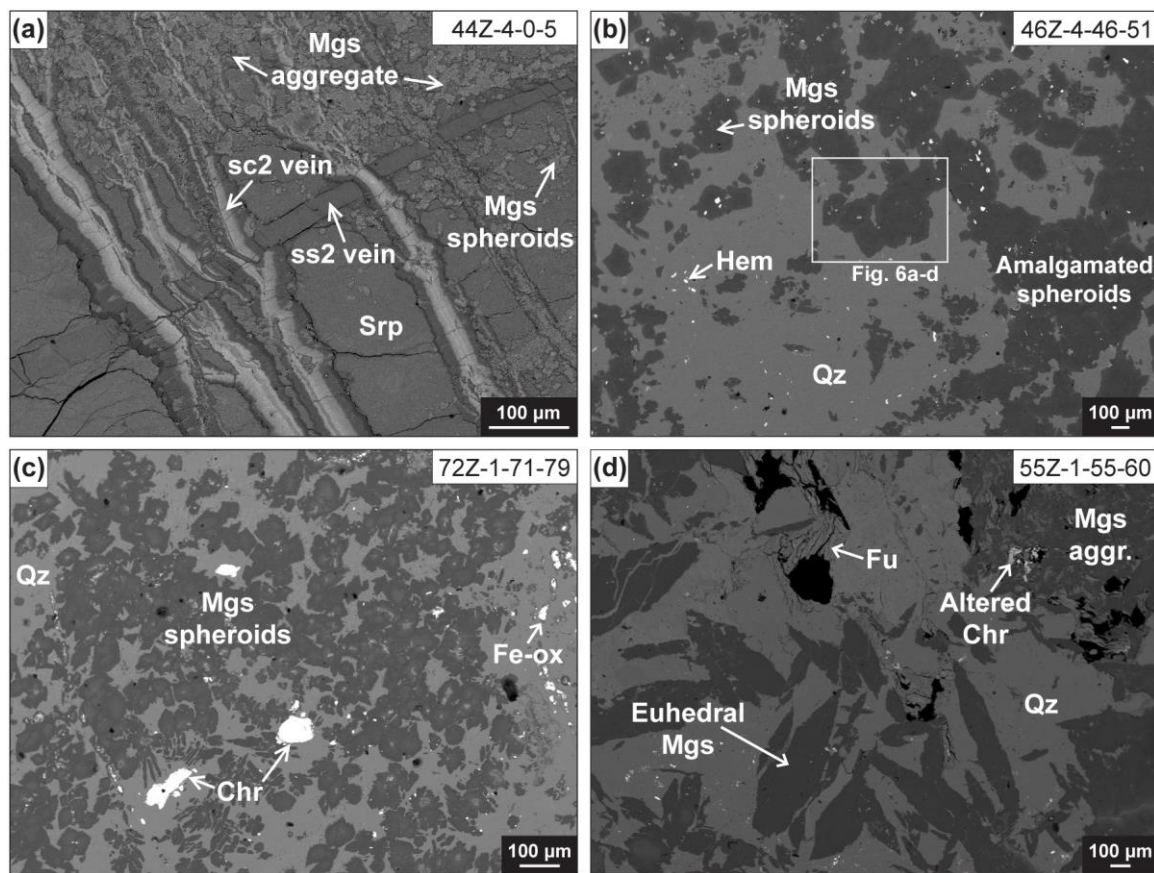


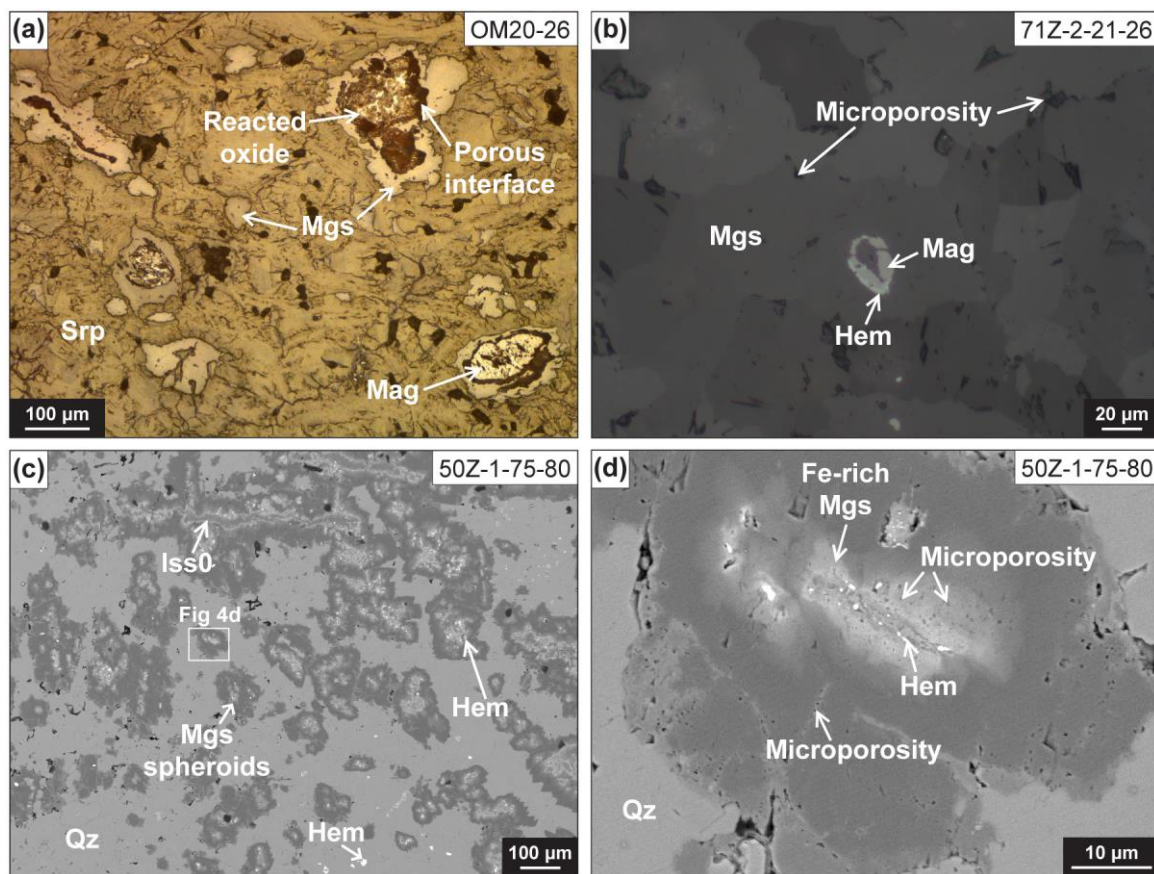
Figure 3: BSE images of chemically zoned magnesite spheroids and veins in (a) carbonated serpentinite (44z-4-0-5) and (b-d) (fuchsite-bearing) listvenite (46z-4-46-51, 72z-1-71-79 and 55z-1-55-60). (a) Crack-seal serpentine vein (ss2) cut by early magnesite vein (sc2) showing a Fe-rich median zone (light grey). Spheroids and aggregates form in the vicinity of sc2 veins. (b) Mg-rich core spheroids, locally amalgamated. (c) Fe-core spheroids (light grey cores). (d) Lens-shaped euhedral magnesite in a fuchsite-bearing sample. Abbreviations: Chr: Cr-spinel, Fe-ox: Fe-oxides, Hem: hematite, Mgs: magnesite, Qz: quartz, Srp: serpentine.

195

Carbonates pervasively replacing the matrix occur as (a) isolated, often clustering, spheroidal to euhedral cores, defined as “spheroids” by Beinlich et al. (2020), and (b) aggregates (Fig. S3). In listvenites, spheroids are composed of magnesite and

200 range in size between 50–300 μm (Figs. 3, 4); they typically display spherical shape locally overgrown by dendritic or euhedral magnesite. In carbonated serpentinites, spheroids are smaller ($<80 \mu\text{m}$) and are composed of magnesite or dolomite. Carbonate aggregates occur as: a) clusters of spheroids, b) pervasive carbonate replacement growing from veins into the matrix within densely veined domains (Fig. S4), and c) pervasive replacement by subhedral to euhedral sub-millimetric magnesite or dolomite (e.g., listvenites 30Z-2-33-39, 55Z-1-55-60; Fig. 3d).

205 The distribution and abundance of matrix carbonates is spatially correlated to the presence and density of the early antitaxial carbonate veins (sc2, lc1; Fig. S3). In carbonated serpentinites, matrix carbonates occur as sparse spheroids or aggregates, frequently in the vicinity of sc2 veins (Fig. 3a). In listvenites, spheroids and aggregates are often abundant close to pseudomorphosed lss0 mesh rims and lc1 veins, although extended matrix replacement in response to advanced carbonation is also observed at distance with veins.



210

215

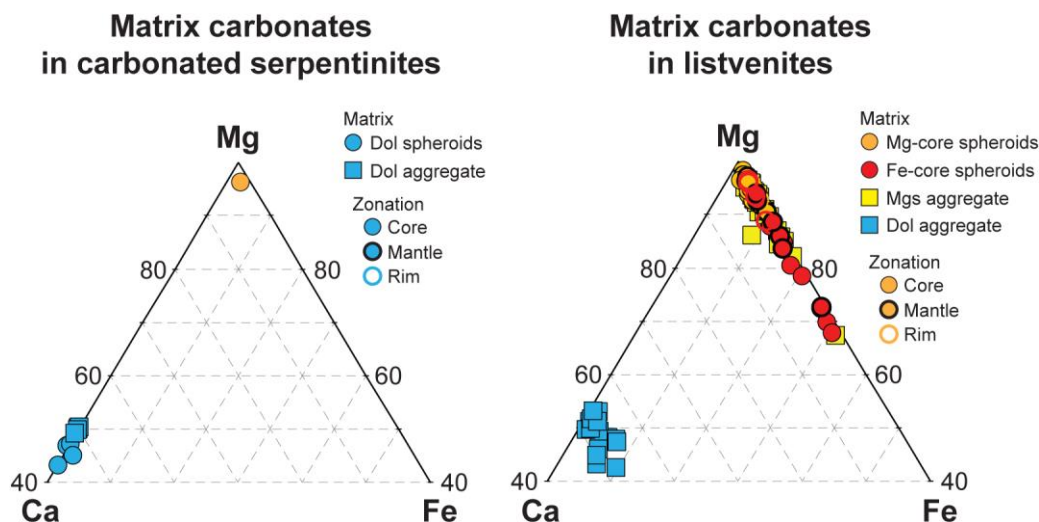
Figure 4: Textural relationships between Fe-oxides and magnesite. (a) Reflected light (RL) image of spheroids in carbonated serpentinite OM20-26. Magnesite surrounding variously reacted Fe-oxides (“reacted oxide”) and magnetite (“Mag”). A porous interface connects oxide relicts and magnesite. (b) Magnetite destabilized into hematite and overgrown by magnesite aggregate in listvenite 71Z-2-21-26. Presence of a microporosity along (sub)grain boundaries. (c) BSE image of Fe-rich core magnesite spheroids close to pseudomorphic magnesite veins (“lss0”) in listvenite 50z-1-75-80. Fe-rich cores (light grey) include fine hematite inclusions. (d) Internal Fe-zoning of Fe-rich core spheroid, with hematite and microporous zone outlining the relict of reacted Fe-oxide. Abbreviations: Hem: hematite, Mgs: magnesite, Qz: quartz, Srp: serpentine.

4.3 Composition and spatial distribution of magnesite spheroids in relation to early antitaxial veins

SEM-EDS mapping and BSE imaging of early carbonate microstructures reveal chemical zoning for matrix and vein
220 magnesites, as illustrated on Ca-Mg-Fe and Si-Ca+Mg-Fe ternary diagrams (Figs. 5, S5, and S6). Magnesite composition
varies mostly between the Mg and Fe solid solution end-members.

Pseudomorphic lss0 and antitaxial sc2/lc1 magnesite veins show Mg-Fe zoning from median zone to vein walls (Figs. 3a).
Median zones are composed of Fe-rich magnesite (X_{Mg} : 0.67-0.87 and 0.57-0.9 in sc2 and lc1 veins, respectively; X_{Mg} : molar
Mg/Mg+Fe); Table S4) compared to vein walls (X_{Mg} : 0.89-0.97 in sc2 and lc1 veins).

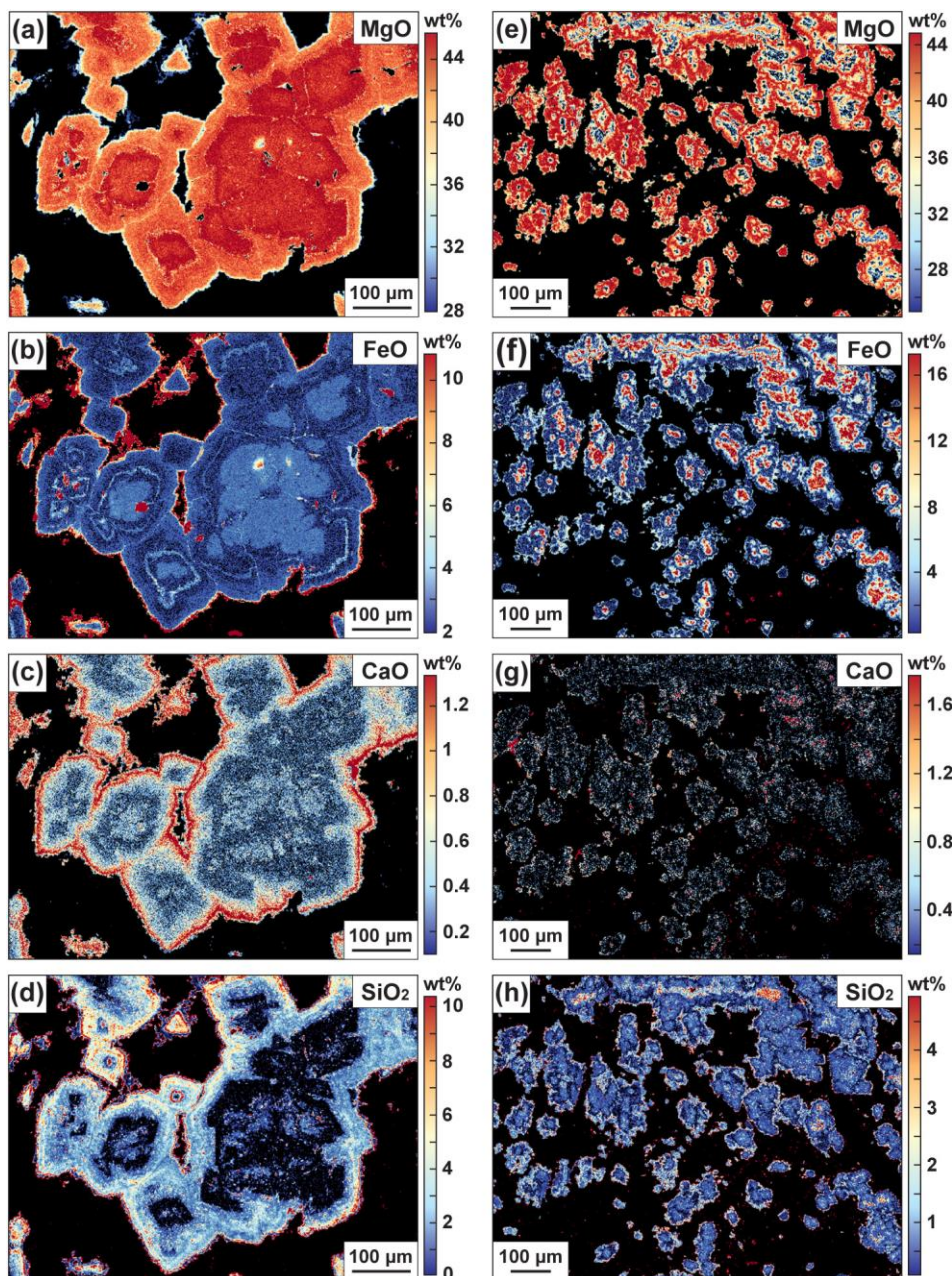
225 For the matrix, we distinguish two types of magnesite spheroids characterized by different core-to-rim Mg-Fe zoning: Mg-rich
core (or Mg-core) and Fe-rich core (or Fe-core) spheroids. Mg-core spheroids (Figs. 3b, 6a-d) have X_{Mg} varying from core
(0.91-0.99) to rim (0.85-0.97) (Fig. 5). Fe-core spheroids (Figs. 3c, 4c-d, 6e-h) display X_{Mg} ranging from 0.69-0.88 (core) to
0.73-0.97 (mantle and rim) (Figs. 5, 6f). Mg core spheroids are the most common but Fe-core spheroids, although less frequent,
230 are present in most of the Fanja listvenites (Table S2). Mg-core spheroids range between 50 and 300 μm in size and they are
observed either in the vicinity of sc2/lc1 veins, but also at distance with veins. They cluster into aggregates in the most densely
veined domains (Fig. S3). Fe-core spheroids are smaller than 100 μm and mostly nucleated in the vicinity of lss0 and lc1 veins,
typically in domains with a low vein density.



235 **Figure 5:** Ternary diagrams of carbonate compositions measured by electron probe micro-analysis (EPMA). Mg, Ca and Fe represent end-members of solid-solutions for carbonates, with magnesite, calcite and siderite as pure phases, respectively. The proportions of each end-member were calculated as the cationic fraction of $M^{2+}/(Fe+Mg+Ca)$ ($M^{2+}=Fe, Mg$ or Ca). Analysed area is indicated for chemically zoned carbonates (core, mantle, rim).

Fe-rich cores are distinguished by the presence of tiny grains of hematite (typical size: $<5 \mu\text{m}$, Fig. 4c-d), and of characteristic destabilization textures around Fe-oxides in listvenites (Fig. 4b-d). Destabilization textures are observed also in spheroid cores
240 in carbonated serpentinites where the development of microporosity at the carbonate-oxide interface is also observed (Fig. 4a).

Magnesite growing after reacted oxides and their microporous corona has the highest Fe compositions (X_{Mg} : 0.69-0.71; Figs. 6f).



245 **Figure 6:** Quantitative element distribution maps of Mg-core (a-d, 46z-4-46-51) and Fe-core spheroids (e-h, 50z-01-75-80) in listvenites. Mapped areas indicated in Fig. 3b and Fig. 4c, respectively.

Another type feature of spheroids is the presence of small domains rich in silica inclusions within cores, and increasing silica content at the rim of spheroids (Fig. 6d, 6h) (Fig S6, Table S4). Silica distribution in spheroids is associated to the presence of nano-inclusions within the lattice of magnesite, with serpentine inclusions in carbonated serpentinites (Beinlich et al., 2020) and SiO₂ inclusions in listvenites (this study, Beinlich et al., 2020; Menzel et al., 2021). All magnesites have low Ca concentrations (<1 wt%; Figs. 5, 6c, 6g) except at the rim (up to 1.2 wt% CaO, this study, Beinlich et al. (2020)), although internal growth of dolomite is observed in rare cases (e.g., listvenite 31Z-3-26-31).

4.4 Transition metals in carbonates

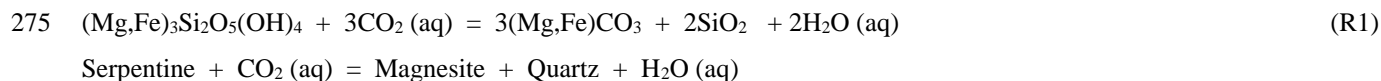
The compositions in transition metals were measured by EPMA (Mn, Cr) and LA-ICP-MS (Sc, Ti, V, Co, Ni, Cu, Zn) for the various carbonate microstructures (Tables S4, S10). The compositions of carbonates are highly scattered for all transition elements, revealing zoning, polymineralic assemblages and/or mineral inclusions (oxides, sulphides, serpentine relics or newly formed quartz) in particular for LA-ICPMS data (100 microns spots). Nevertheless, global trends characterizing the different lithologies and textures can be identified using median compositions (Table S11).

In carbonated serpentinites, listvenites and fuchsite-bearing listvenites, matrix carbonates (spheroids and aggregates) are overall enriched in elements concentrated in serpentinitized peridotites (Fe and transition metals) when compared to veins (e.g., in carbonated serpentinites, median Ni is ~840 ppm and ~500 ppm in matrix and vein carbonates, respectively). The efficient trapping of protolith-derived elements suggests fast carbonation kinetics with respect to elemental transport when spheroids and aggregates were formed, in contrast to fluid dominated carbonate veins. In both veins and matrix, dolomite shows an affinity for Sc, while magnesite preferentially incorporates Co and has the highest Fe/Mn ratios. The distribution of remaining transition elements varies from carbonated serpentinites to listvenites and fuchsite-bearing listvenites. Matrix carbonates are overall enriched in Ni, Cu and Zn and depleted in Ti in carbonated serpentinites and fuchsite-bearing listvenites when compared to listvenites. We identified also variations in the magnesite compositions with changes in the matrix textures. Magnesite aggregates are distinguished from Mg-core spheroids by their higher Mn compositions. The Fe-core spheroids are characterized by their high Ti, V, Co, Cu and Zn compared to Mg-core spheroids and magnesite aggregates.

270 5 Discussion

5.1 Carbonation sequence and conditions of listvenite formation

The Fanja region exposes a suite of listvenites resulting from the carbonation of serpentinitized peridotites at the base of the ophiolite mantle. This reaction can be written as a single reaction (Johannes, 1969):



The investigated sites indicate however that carbonation occurred over several stages and/or following different reaction pathways: Sites 1 and 2 record carbonation reactions from serpentinized peridotites to carbonated serpentinites and minor listvenites, while BT1B cores preserve the transition from carbonated serpentinites to listvenites and fuchsite-bearing listvenites. The Fanja carbonated serpentinites and listvenites are characterized by highly variable proportions of Mg-carbonates and silicates at the sample scale yet bulk rock studies show that they preserve the geochemical signatures of the Semail ophiolite mantle at the metre to borehole scale (Falk and Kelemen, 2015; Godard et al., 2021; Okazaki et al., 2021). So, except for the addition of CO₂ and release of water (R1) and the minor addition of Ca and selected fluid-mobile elements (Godard et al., 2021), carbonation reactions could be considered as mass conservative.

In contrast, at the microscopic scale, petrographic, mineral and chemical investigations show the development of a complex sequence of veining, mineral dissolution and growth, and elemental redistribution. We identified 5 distinctive stages of carbonation reactions: 1) the pseudomorphic replacement of serpentine mesh rims and veins (sc0, lss0, lss2) and the generation of early antitaxial Fe-rich magnesite veins (sc2 and lc1); 2) the growth of Fe-rich magnesite forming cores of spheroids and aggregates in the vicinity of mesh rims and antitaxial veins; 3) the formation of Mg-rich magnesite forming spheroids, aggregates and overgrowths on pre-existing microstructures; 4) silicification; 5) late generation of carbonate and quartz-bearing syntaxial veins, later cut by or cutting cataclasites.

Magnesite having variable Fe contents have been reported in listvenites from the Linnajavri Ultramafic Complex (Tominaga et al., 2017) and in the Advocate Ophiolite (Menzel et al., 2018) and interpreted as revealing changes in the local redox conditions (e.g., Frost, 1985). However, the widespread preservation of Fe-rich magnesites formed during incipient carbonation distinguishes the Fanja samples from previously investigated listvenites.

This suite of features could point to changes in the pressure and temperature conditions as carbonation progressed. Petrology and thermometry studies of the Fanja region indicate carbonation temperatures below 200°C (Kelemen et al., 2022), and more precisely of 90±15°C for regional samples (Falk and Kelemen, 2015) and from 247±52 to 45±5 °C for Hole BT1B (Beinlich et al., 2020), suggesting that carbonation occurred during cooling of the Semail mantle lithosphere. The depth at which the reaction proceeded is not well constrained: less than 40 km if assuming a cold subduction zone setting (Kelemen et al., 2022), or calculated depth of ~3.75-7.5 km based on clumped isotopes temperatures and a relatively warm geotherm (Beinlich et al., 2020; outlier temperatures not considered). For discussion, we here consider pressures of ~125–300 MPa and temperatures of 100-200°C consistent with ophiolite obduction and cooling (Beinlich et al., 2020), but we note that pressures may have been higher.

Mineral assemblages formed during peridotite carbonation and their compositions are not very sensitive to pressure (Johannes, 1969). Activities of dissolved silica and CO₂ in fluids are independent on pressure variation (10-100 MPa, Klein and Garrido, 2011). Decreasing pressure favours stabilization of the quartz–magnesite assemblage at lower fluid XCO₂ composition (XCO₂: molar CO₂ fraction of a binary H₂O-CO₂ fluid) (Menzel et al., 2018). Temperature variation, on the other hand, has a strong

310 effect on activities (Klein and Garrido, 2011), also impacting fluid properties such as the solubility of magnesite and siderite (Bénézech et al., 2009, 2011). X_{Mg} of magnesite varies as function of changes in phase assemblages during temperature decrease, in particular in relation with magnetite conversion to hematite (Menzel et al., 2018).

Changes in the compositions of the inlet CO₂-bearing fluids as documented along Hole BT1B (Carter et al, 2020; de Obeso et al, 2022) may also have led to variable reaction pathways (e.g., dolomite predominates in Ca-enriched zones along Hole BT1B 315 (Godard et al, 2021)). Finally, the formation of Fe- to Mg-rich magnesites suggests changes in the mobility, partitioning and oxidation state of this element during carbonation progress. Thereafter, we discuss the possible roles of these different parameters in the development of matrix replacement textures and compositional features.

5.2 Matrix replacement textures: role of oxides

Pervasive matrix carbonation appears to have occurred principally according to reaction R1, with the formation of abundant 320 Mg-core spheroids and Mg-rich magnesite aggregates, with measured compositions similar to those predicted by Klein and Garrido (2011). In contrast, incipient matrix replacement by magnesite proceeds with the formation of Fe-core spheroids and Fe-rich magnesite aggregates, localized to the vicinity of lss0 and lc1 veins. Fe partitioning in the Fanja samples is likely controlled dominantly by the mineralogy and stability of Fe-bearing minerals (Fe-oxides, magnesite and, when present, serpentine and Fe-sulphides). Our samples preserve textural evidences suggesting the formation of magnesite after magnetite 325 in carbonated serpentinites (Fig. 4a) and listvenites (Fig. 4b), with locally the preservation of microporous interfaces. These mineral assemblages are commonly associated to tiny hematite grains (Fig. 4c-d). We propose that Fe-rich spheroids could represent the end-product of this reaction as suggested also by their relatively high contents in transition metals typically concentrated in oxides (Table S7).

The destabilization of magnetite in presence of CO₂-rich fluids to form Fe-rich carbonate (siderite) has been proposed by Frost 330 (1985):



335 Reaction R2 will produce an increase in oxygen fugacity. However, O_{2, (aq)} solubility is negligible in hydrothermal aqueous fluids at the P-T conditions of the Fanja listvenite formation. Therefore, reaction R2 will not occur unless it is buffered by a coupled oxidation reaction such as:



These coupled reactions could account for the association of destabilized magnetite, Fe-rich magnesite and hematite in our samples. Assuming the absence of reduced fluid species and no change in bulk rock $\text{Fe}^{3+}/\text{Fe}_{\text{TOT}}$ (redox neutral system), they could be rewritten as:

345



where R4 acts as a redox buffer. The observation of Fe-oxide inclusions in magnesite, where relict magnetite is replaced by hematite (Fig. 4b), is consistent with reaction R4.

350

Thereafter, we use thermodynamic modelling as a supporting tool to discuss the different parameters explaining the formation of Mg-core and Fe-core spheroids during carbonation reactions, mainly fluid XCO_2 composition, redox conditions at P-T conditions consistent with ophiolite cooling (Beinlich et al., 2020).

5.3 Role of the fluid composition and redox conditions

355 In order to better understand the role of different initial redox conditions and possible redox changes during carbonation reaction progress, we applied thermodynamic modelling using *Perple_X*. We calculated $\text{Fe}^{3+}/\text{Fe}_{\text{TOT}}\text{-XCO}_2$ pseudosections (Fig. 7a) for a simplified harzburgite bulk composition (based on OM94-52h by Hanghøj et al., 2010) with binary compositional mixing from reduced to fully oxidized with saturated H_2O and CO_2 , as harzburgite is the dominant lithology in the Semail mantle section. Pressure and temperature were fixed at 0.3 GPa and 200°C and serpentine was modelled by antigorite (Atg). The model assumes a simplified rock-buffered FMS-COH, fluid-saturated system, accounting for phase assemblages composed of magnesite, quartz, serpentine, talc, magnetite, and hematite (see Methods for further calculation details).

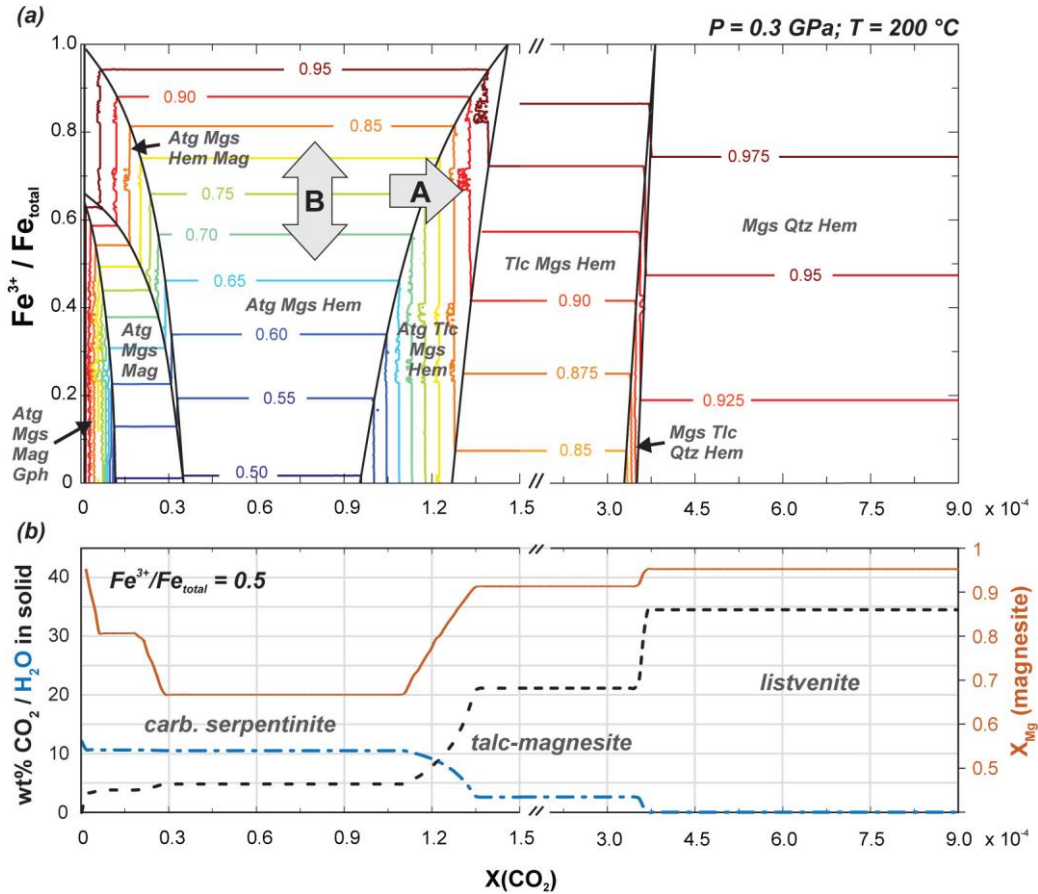
360

Although Fig. 7 is based strictly on an equilibrium model where the fluid composition is rock-buffered, this model can provide useful insights into progressive carbonation of serpentinite and Fe partitioning during this process (Frost, 1985; Menzel et al., 2018), albeit with some caveats. For example, fluid XCO_2 in Fig. 7 does not correspond to that of an infiltrating fluid, but to the CO_2 concentration that a fluid would acquire once equilibrated with mineral assemblages. If fluid fluxes are high and CO_2 renewal fast, the buffering capacity of the local mineral assemblage may be kinetically overstepped and reactions and fluid composition may become controlled predominantly by the infiltrating fluid. Such an overstepping and kinetic inhibition of talc formation at low temperatures may explain (i) the scarcity of talc-magnesite assemblages in Hole BT1B although equilibrium models predict a rather wide range of XCO_2 for talc stability, and (ii) the presence of disequilibrium assemblages such as serpentine–quartz–magnesite, as observed in some carbonated serpentinites in Hole BT1B (Menzel et al., 2022). Also, because the model considers full equilibration of all mineral phases, it cannot account for Fe-zoning in magnesite where cores are

370

isolated and do not equilibrate. Isolated core compositions can still be predicted under the assumption that they formed during incipient reaction steps that correspond to mineral assemblages with stable serpentine.

375 Figure 7a illustrates the two endmember reaction pathways that can produce Fe-rich and Mg-rich magnesite (here expressed as X_{Mg} at constant P–T conditions: (A) a change in phase assemblage and magnesite abundance with progressive carbonation and correspondingly increasing rock-buffered XCO_2 at constant redox (constant Fe^{3+}/Fe_{TOT}), corresponding to buffering of the system through R4; and (B) a change of the bulk redox with increasing Fe^{3+}/Fe_{TOT} in case of oxidation or decreasing Fe^{3+}/Fe_{TOT} in case of reduction (cf. arrows in Fig. 7a).



380

Figure 7: Model of Fe-partitioning in relation to carbonation and bulk rock redox budget. (a) Isobaric and isothermal, fluid-saturated, Fe^{3+}/Fe_{tot} - XCO_2 pseudosection in the FMS-COH system for a harzburgite bulk rock composition with predicted X_{Mg} compositions of magnesite shown as coloured isopleths. (b) Corresponding plot of X_{Mg} of magnesite and CO_2 , H_2O content in solid assemblage at $Fe^{3+}/Fe_{tot} = 0.5$, illustrating the expected magnesite zoning pattern for the case of redox-neutral carbonation. Modelling was done using a simplified hydrated harzburgite composition with binary compositional mixing from reduced ($SiO_2 - 38.77 \text{ wt\%}$; $MgO - 39.21 \text{ wt\%}$; $FeO - 6.99 \text{ wt\%}$) to fully oxidized ($SiO_2 - 38.77 \text{ wt\%}$; $MgO - 39.21 \text{ wt\%}$; $Fe_2O_3 - 7.77 \text{ wt\%}$) with saturated H_2O and CO_2 . For illustration purposes the results of two calculations at the same conditions but different ranges of XCO_2 were combined (note change in scaling of the x-axis).

385

Exemplary for case A, the evolution of X_{Mg} in magnesite with increasing XCO_2 for an average bulk rock Fe^{3+}/Fe_{TOT} of 0.5 is shown in Fig. 7b. High Fe content of magnesite in the Atg–Mgs–Hem stability field ($X_{Mg} = 0.7$) is consistent with some

390 measured magnesite core compositions in serpentinite (Fig. S6) and Fe-core spheroids preserved in listvenite (Fig. 6). Likewise, at high fluid X_{CO_2} , the precipitation of Mg-rich magnesite is expected, consistent with the compositions of Mg-core spheroids and overgrowths in listvenite (Fig. 6). This suggests that, to a large extent, compositional zoning is the result of Fe redistribution during magnetite breakdown and increasing magnesite abundance with progressive carbonation. Alternatively, Mg-core spheroids may form after a highly oxidized protolith, or precipitation in a rock domain with locally
395 low Fe_{TOT} contents, or extreme overstepping of reaction such that magnesite compositions could not equilibrate according to serpentinite-bearing phase assemblages but were fully determined by high X_{CO_2} of the infiltrating fluid.

Regarding case B, the model predicts lower X_{Mg} of magnesite for reduced bulk compositions with low Fe^{3+}/Fe_{TOT} . This is very pronounced for assemblages where serpentinite is stable, whereas in listvenite (Mgs–Qtz–Hem assemblage at high X_{CO_2}) changes in bulk rock Fe^{3+}/Fe_{TOT} are predicted to have only a minor effect on magnesite X_{Mg} because Fe is diluted within >
400 65% mol% of magnesite in the assemblage. Thus, two effects may substantially influence the compositional zoning patterns that can develop during carbonation progress: changes in redox budget induced by the infiltrating fluids, and the initial Fe^{3+}/Fe_{TOT} of the protolith serpentinite or partially serpentinitized peridotite. Bulk Fe^{3+}/Fe_{TOT} ratios for serpentinitized peridotites in Oman are 0.4-0.55 (Mayhew et al., 2018), and varying between 0.3-0.74 for carbonated serpentinites and 0.13-0.61 for listvenites in Hole BT1B (Godard et al., 2021). As shown in Fig. 7a, magnesite in the serpentinite stability fields is predicted to
405 be very rich in Fe for protoliths with low Fe^{3+}/Fe_{TOT} ($X_{Mg} < 0.6$) but only moderately Fe-bearing in oxidized bulk compositions. The formation of Mg-core and Fe-core spheroids (Fig. 6) may thus be due to a variability of the protolith Fe^{3+}/Fe_{TOT} , assuming that the core magnesite compositions of spheroids in listvenites correspond to an early carbonation reaction stage when serpentinite was stable.

Interestingly, independently of the initial bulk Fe^{3+}/Fe_{TOT} , complete transformation of magnetite to hematite and Fe-bearing
410 magnesite is predicted to occur with relatively minor magnesite precipitation in assemblages with serpentinite at low X_{CO_2} . As a consequence of magnetite destabilization, the conversion of peridotite to listvenite is generally accompanied by a decrease in bulk Fe^{3+}/Fe_{TOT} (e.g. Menzel et al., 2018), and magnetic susceptibility (Tominaga et al., 2017).

6 Summary and implications

The petrological study of carbonated serpentinites and listvenites highlighted the widespread occurrence of Fe-zoning in matrix
415 and vein magnesite arising during incipient carbonation of serpentinitized peridotites. The pervasive replacement of serpentinite by magnesite is characterized by the formation of spheroids, among which two types were identified based on the composition of their core regions: Mg-core and Fe-core spheroids.

We document for the first time in detail the different carbonation reactions destabilizing Fe-oxides into Fe-rich magnesite and consistent with a self-buffered reaction corresponding to the conversion of magnetite into Fe-rich magnesite and hematite.
420 Thermodynamic modelling converges to the precipitation of Fe-rich magnesite in the presence of metastable serpentinite, also

dependent on fluid XCO₂ composition and local redox conditions. Fe-rich cores thus record a transient step of carbonation, followed by the pervasive (over)growth of Mg-rich spheroids and aggregates under increased fluid supply.

Even though present in a majority of our listvenite samples, the scarcity of Fe-core spheroids compared to Mg-rich matrix magnesite may be a hint for fast transition from limited to intensive fluxing of reactive fluids. This transition may be caused
425 by cyclic fluid pressure variations under regional tectonic stress, related to reaction-enhanced deformation (Menzel et al., 2021) and reaction-induced fracturing (e.g. Kelemen et al., 2022).

Carbonation triggers the destabilization of Fe-oxides, thereby influencing the partitioning of iron between minerals, and induces changes of the redox conditions. In the Fanja samples, carbonation of serpentinized peridotite to listvenite is accompanied by evolving assemblages of Fe-oxides and sulphides. The association of magnetite–awaruite identified in slightly
430 carbonated serpentinites equilibrates in highly reducing conditions during serpentinization (Klein and Bach, 2009; de Obeso et al., 2020), while the conversion to rare Fe-Cu rich sulphides and abundant hematite point to a change to oxidizing conditions (Eckstrand, 1975; Frost et al., 1985).

Sulphides generally lack in the Fanja samples, whilst commonly observed in other occurrences of (ore-bearing) listvenites elsewhere (e.g. Qiu and Zhu, 2018). Scarcity or absence may result from oxidation of sulphide to highly soluble sulphate, as
435 similarly proposed for fuchsite-bearing listvenites at the Gråberget ultramafic body (Austrheim et al., 2021). These reactions may participate to the mobilization of trace-metals (especially Ni, Co and Cu), but potentially also affecting the speciation of carbon, sulphur and hydrogen (e.g., Frost et al., 1985; Frost and Beard, 2007). These implications have to be considered for mass transfers at a larger-scale, as listvenite formation is inferred to occur along basal sections of obducted ophiolites and in the shallow mantle wedge of subduction zones (Kelemen and Manning, 2015), with potential impact on the cycling of redox-
440 sensitive elements and metals.

Data availability

All data is contained in the figures of the manuscript and supplementary information; raw images of these figures are available from the authors upon request. Data will be available online on the PANGAEA data repository.

Sample availability

445 Archive halves and samples of BT1B cores are available through the Oman Drilling Project (<https://www.omandrilling.ac.uk/samples-data>). Archive samples from Site 1 and Site 2, and all studied thin sections are stored at the Géosciences Montpellier.

Author contribution

This work is part of TD's PhD thesis at Géosciences Montpellier. MG designed the project. TD, EO and RL conducted field
450 work. TD and EO refined geological maps. TD, MG, FP and MM studied the petrography and the petrology. TD performed
SEM imaging, EDX mapping, EPMA and LA-ICP-MS data acquisition and treatment, image processing, and drafted the
figures. FB conducted EDS analyses. MM performed thermodynamic modelling. All authors discussed and interpreted the
results. TD and MG led the writing of the manuscript, to which all authors contributed.

Competing interests

455 The authors declare that they have no conflict of interest.

Acknowledgments

We thank Othmar Müntener, Martin Robyr, Alexey Ulianov and Olivier Reubi for allowing an access to the laboratory facilities
at the University of Lausanne during the COVID-19 pandemic. This work benefited from constructive and appreciated
discussions with Françoise Boudier. We thank the Sultanate of Oman Public Authority for Mining for support to conduct
460 fieldwork and export samples. We also thank Sobhi Nasir for his support during fieldtrip in Oman.

This research used core samples provided by the Oman Drilling Project. The Oman Drilling Project (OmanDP) has been
possible through co-mingled funds from the International Continental Scientific Drilling Project (ICDP; Kelemen, Matter,
Teagle Lead PIs), the Sloan Foundation – Deep Carbon Observatory (Grant 2014-3-01, Kelemen PI), the National Science
Foundation (NSF-EAR-1516300, Kelemen Lead PI), NASA – Astrobiology Institute (NNA15BB02A, Templeton PI), the
465 German Research Foundation (DFG: KO 1723/21-1, Koepke PI), the Japanese Society for the Promotion of Science (JSPS
no:16H06347, Michibayashi PI; and KAKENHI 16H02742, Takazawa PI), the European Research Council (Adv: no.669972;
Jamtveit PI), the Swiss National Science Foundation (SNF:20FI21_163073, Früh-Green PI), JAMSTEC, the TAMU-JR
Science Operator, and contributions from the Sultanate of Oman Ministry of Regional Municipalities and Water Resources,
the Oman Public Authority of Mining, Sultan Qaboos University, CNRS-Univ. Montpellier, Columbia University of New
470 York, and the University of Southampton.

This study was funded by Project ANR-18-CE01-0014-01 LISZT.

References

Alt, J.C., Schwarzenbach, E.M., Früh-Green, G.L., Shanks, W.C., Bernasconi, S.M., Garrido, C.J., Crispini, L., Gaggero, L.,
Padrón-Navarta, J.A., and Marchesi, C.: The role of serpentinites in cycling of carbon and sulfur: Seafloor serpentinitization
475 and subduction metamorphism, *Lithos*, 178, 40-54, doi:10.1016/j.lithos.2012.12.006, 2013.

- Aftabi, A., and Zarrinkoub, M.H.: Petrogeochemistry of listvenite association in metaophiolites of Sahlabad region, eastern Iran: Implications for possible epigenetic Cu–Au ore exploration in metaophiolites, *Lithos*, 156-159, 186-203, doi:10.1016/j.lithos.2012.11.006, 2013.
- Austrheim, H., Corfu, F., and Renggli, C.J.: From peridotite to fuchsite bearing quartzite via carbonation and weathering: with implications for the Pb budget of continental crust, *Contrib. Mineral. Petrol.*, 176, 94, doi: 10.1007/s00410-021-01851-z, 2021.
- 480 Bechenec, F., Le Metour, J., Rabu, D., Bourdillon-de-Grissac, C., de Wever, P., Beurrier, M., and Villey, M.: The Hawasina Nappes: stratigraphy, palaeogeography and structural evolution of a fragment of the south-Tethyan passive continental margin, *Geol. Soc. Spec. Publ.*, 49, 213-223, doi:10.1144/gsl.sp.1992.049.01.14, 1990.
- Beinlich, A., Plümper, O., Hövelmann, J., Austrheim, H., and Jamtveit, B.: Massive serpentinite carbonation at Linnajavri, N–
485 Norway, *Terra Nova*, 24(6), 446-455, doi: 10.1111/j.1365-3121.2012.01083.x, 2012.
- Beinlich, A., Plümper, O., Boter, E., Müller, I. A., Kourim, F., Ziegler, M., Harigane, Y., Lafay, R., and Kelemen, P.B., & the Oman Drilling Project Science Team: Ultramafic rock carbonation: Constraints from listvenite core BT1B, Oman drilling project, *J. Geophys. Res. Solid Earth*, 125, e2019JB019060, doi:10.1029/2019JB019060, 2020.
- Bénézech, P., Dandurand, J.L., and Harrichoury, J.C.: Solubility product of siderite (FeCO₃) as a function of temperature (25–
490 250 °C), *Chem. Geol.*, 265, 3-12, doi:10.1016/j.chemgeo.2009.03.015, 2009.
- Bénézech, P., Saldi, G., Dandurand, J.L., and Schott, J.: Experimental determination of the solubility product of magnesite at 50 to 200 °C, doi: 10.1016/j.chemgeo.2011.04.016, 2011.
- Boudier, F., Ceuleneer, G., and Nicolas, A.: Shear zones, thrusts and related magmatism in the Oman ophiolite: Initiation of thrusting on an oceanic ridge, *Tectonophysics*, 151(1-4), 275-296, doi:10.1016/0040-1951(88)90249-1, 1988.
- 495 Boudier, F., and Nicolas, A.: Synchronous Seafloor Spreading and Subduction at the Paleo-Convergent Margin of Semail and Arabia, *Tectonics*, 37, 2961-2982, doi:10.1029/2018TC005099, 2018.
- Boudier, F., Baronnet, A., and Mainprice, D. (2010). Serpentine mineral replacements of natural olivine and their seismic implications: Oceanic lizardite versus subduction-related antigorite. *Journal of Petrology*, 51(1–2), 495–512, doi:10.1093/petrology/egp049, 2010.
- 500 Bouilhol, P., Debret, B., Inglis, E.C., Warembourg, M., Grocolas, T., Rigaudier, T., Villeneuve, J., and Burton, K.W.: Decoupling of inorganic and organic carbon during slab mantle devolatilisation, *Nat. Commun.*, 13, 308, doi: 10.1038/s41467-022-27970-0, 2022.
- Boskabadi, A., Pitcairn, I.K., Leybourne, M.I., Teagle, D.A.H., Cooper, M.J., Hadizadeh, H., Bezenjani, R.N., and Bagherzadeh, R.M.: Carbonation of ophiolitic ultramafic rocks: Listvenite formation in the Late Cretaceous ophiolites of
505 eastern Iran, *Lithos*, 352-353, 105307, doi:10.1016/j.lithos.2019.105307, 2020.
- Carter, E.: Ophiolites as archives of hydration, carbonation and metasomatic processes in the oceanic lithosphere: insights from halogen and noble gas systematics, Ph.D. Thesis, Department of Earth and Environmental Sciences, University of Manchester, 305 p., 2020.

- Coleman, R.: Tectonic setting for ophiolite obduction in Oman, *J. Geophys. Res. Solid Earth*, 86, 2497-2508, doi:10.1029/JB086iB04p02497, 1981.
- 510 Connolly, J.A.D.: Computation of phase equilibria by linear programming: A tool for geodynamic modeling and its application to subduction zone decarbonation, *Earth Planet. Sci. Lett.*, 236, 524-541, doi: 10.1016/j.epsl.2005.04.033, 2005.
- Connolly, J.A.D.: The geodynamic equation of state: What and how, *Geochem. Geophys.*, 10, Q10014, doi: 10.1029/2009GC002540, 2009.
- 515 de Obeso J.C., and Kelemen, P.B.: Major element mobility during serpentinization, oxidation and weathering of mantle peridotite at low temperatures, *Phil. Trans. R. Soc. A*, 378, 20180433, doi:10.1098/rsta.2018.0433, 2020.
- Debret, B., Bouilhol, P., Pons, M.L., and Williams, H.: Carbonate Transfer during the Onset of Slab Devolatilization: New Insights from Fe and Zn Stable Isotopes, *J. Petrol.*, 59, 1145-1166, doi:10.1093/petrology/egy057, 2018.
- Delacour, A., Früh-Green, G.L., Bernasconi, S.M., Schaeffer, P., and Kelley, D.S.: Carbon geochemistry of serpentinites in the Lost City Hydrothermal System (30°N, MAR), *Geochim. Cosmochim. Acta*, 72, 3681-3702, doi:10.1016/j.gca.2008.04.039, 2008.
- 520 Deschamps, F., Godard, M., Guillot, S., and Hattori, K.: Geochemistry of subduction zone serpentinites: A review, *Lithos*, 178, 96-127, doi:10.1016/j.lithos.2013.05.019, 2013.
- Eckstrand, O.R.: The Dumont serpentinite; a model for control of nickeliferous opaque mineral assemblages by alteration reactions in ultramafic rocks, *Econ. Geol.*, 70(1), doi:10.2113/gsecongeo.70.1.183, 1975.
- 525 Falk, E.S., and Kelemen P.B.: Geochemistry and petrology of listvenite in the Samail ophiolite, Sultanate of Oman: Complete carbonation of peridotite during ophiolite emplacement, *Geochim. Cosmochim. Acta*, 160, 70-90, doi:10.1016/j.gca.2015.03.014; 2015.
- Frost, B.R.: On the Stability of Sulfides, Oxides, and Native Metals in Serpentinite, *J. Petrol.*, 26(1), 31-63, doi: 10.1093/petrology/26.1.31, 1985.
- 530 Frost, B.R., and Beard, J.S.: On Silica Activity and Serpentinization, *J. Petrol.*, 48(7), 1351-1368, doi: 10.1093/petrology/egm021, 2007.
- Garber, J.M., Rioux, M., Searle, M.P., Kylander-Clark, A.R.C., Hacker, B.R., Vervoort, J.D., Warren, C.J., and Smye, A.J.: Dating continental subduction beneath the Samail Ophiolite: Garnet, zircon, and rutile petrochronology of the As Sifah eclogites, NE Oman. *J. Geophys. Res. Solid Earth*, 126, e2021JB022715, doi: 10.1029/2021JB022715, 2021.
- 535 Glennie, K.W., Boeuf, M.G.A., Hugues Clark, M.W., Moody-Stuart, M., Pilaar, W.F.H., and Reinhardt, B.M.: Geology of the Oman Mountains, *Neder. Mijn. Geol. Genoot.*, Delft, Netherlands, 423 pp., 1974.
- Godard, M., Jousset, D., and Bodinier, J.-L.: Relationships between geochemistry and structure beneath a paleo-spreading centre: a study of the mantle section in the Oman ophiolite, *Earth Planet. Sci. Lett.*, 180, 133-148, doi: 10.1016/S0012-821X(00)00149-7, 2000.
- 540

- Godard, M., Carter, E.J., Decrausaz, T., Lafay, R., Bennett, E., Kourim, F., de Obeso, J.C., Michibayashi, K., Harris, M., Coggon, J., Teagle, D., Kelemen, P., and the Oman Drilling Project Phase 1 Science Party: Geochemical Profiles Across the Listvenite-Metamorphic Transition in the Basal Megathrust of the Semail Ophiolite: Results from Drilling at Oman DP Hole BT1B, *J. Geophys. Res. Solid Earth*, 126, e2021JB022733, doi:10.1029/2021JB022733, 2021.
- 545 Griffin, W., Powell, W., Pearson, N.J., and O'Reilly, S.: GLITTER: data reduction software for laser ablation ICP-MS, *Short Course Series*, 40, 308-311, 2008.
- Halls, C., and Zhao, R.: Listvenite and related rocks: perspectives on terminology and mineralogy with reference to an occurrence at Cregganbaun, Co. Mayo, Republic of Ireland. *Mineral. Deposita*, 30, 303-313, doi:10.1007/BF00196366, 1995.
- Hanghøj, K., Kelemen, P.B., Hassler, D., and Godard, M.: Composition and Genesis of Depleted Mantle Peridotites from the Wadi Tayin Massif, Oman Ophiolite; Major and Trace Element Geochemistry, and Os Isotope and PGE Systematics, *J. Petrol.*, 51(1-2), 201-227, doi:10.1093/petrology/egp077, 2010.
- 550 Hansen, L.D., Dipple, G.M., Gordon, T.M., and Kellett, D.A.: Carbonated serpentinite (listwanite) at Atlin, British Columbia: a geological analogue to carbon dioxide sequestration, *Can. Mineral.*, 43(1), 225-239, doi:10.2113/gscanmin.43.1.225, 2015.
- Hinsken, T., Bröcker, M., Strauss, H., and Bulle, F.: Geochemical, isotopic and geochronological characterization of listvenite from the Upper Unit on Tinos, Cyclades, Greece, *Lithos*, 282-283, 281-297, doi:10.1016/j.lithos.2017.02.019, 2017.
- 555 Holland, T.J.B., and Powell, R.: An internally consistent thermodynamic data set for phases of petrological interest, *J. Metamorph. Geol.*, 16, 309-343, doi:10.1111/j.1525-1314.1998.00140.x, 1998.
- Holland, T. and Powell, R.: An improved and extended internally consistent thermodynamic dataset for phases of petrological interest, involving a new equation of state for solids, *J. Metamorph. Geol.*, 29, 333-383, doi:10.1111/j.1525-1314.2010.00923.x, 2011.
- 560 Johannes, W.: An experimental investigation of the system MgO-SiO₂-H₂O-CO₂, *Am. J. Sci.*, 267(9), 1083-1104, doi:10.2475/ajs.267.9.1083, 1969.
- Kelemen, P.B., and Matter, J.M.: In situ carbonation of peridotite for CO₂ storage, *Proc. Natl. Acad. Sci*, 105(45), 17295-17300, doi:10.1073/pnas.0805794105, 2008.
- 565 Kelemen, P.B., and Hirth, G.: Reaction-driven cracking during retrograde metamorphism: Olivine hydration and carbonation, *Earth Planet. Sci. Lett.*, 345-348, 81-89, doi:10.1016/j.epsl.2012.06.018, 2012.
- Kelemen, P.B., and Manning, C.E.: Reevaluating carbon fluxes in subduction zones, what goes down, mostly comes up, *Proc. Natl. Acad. Sci*, 112(30), doi:10.1073/pnas.1507889112, 2015.
- Kelemen, P.B., Matter, J.M., Teagle, D.A.H., Coggon, J.A., and the Oman Drilling Project Science Team: Site BT1: fluid and mass exchange on a subduction zone plate boundary, in: *Proceedings of the Oman Drilling Project*, College Station, Texas (International Ocean Discovery Program), doi:10.14379/OmanDP.proc.2020, 2020.
- 570 Kelemen, P.B., de Obeso, J.C., Leong, J.A., Godard, M., Okazaki, K., Kotowski, A.J., Manning, C.E., Ellison, E.T., Menzel, M.D., Urai, J.L., Hirth, G., Rioux, M., Stockli, D.F., Lafay, R., Beinlich, A.M., Coggon, J.A., Warsi, N.H., Matter, J.M.,

- Teagle, D.A.H., Harris, M., Michibayashi, K., Takazawa, E., Al Sulaimani, Z., and the Oman Drilling Project Science Team:
575 Listvenite formation during mass transfer into the leading edge of the mantle wedge: Initial results from Oman Drilling Project Hole BT1B, *J. Geophys. Res. Solid Earth*, 127, e2021JB022352, doi:10.1029/2021JB022352, 2022.
- Khedr, M. Z., Arai, S. and Python, M.: Petrology and chemistry of basal lherzolites above the metamorphic sole from Wadi Sarami central Oman ophiolite, *J. Mineral. Petrol. Sci.*, 108, 13-24, doi:10.2465/jmps.121026, 2013.
- Klein, F., and Bach, W.: Fe–Ni–Co–O–S Phase Relations in Peridotite–Seawater Interactions, *J. Petrol.*, 50(1), 37-59,
580 doi:10.1093/petrology/egn071, 2009.
- Klein, F., and Garrido, C.J.: Thermodynamic constraints on mineral carbonation of serpentinized peridotite, *Lithos*, 126, 147-160,
doi:10.1016/j.lithos.2011.07.020, 2011.
- Lanari, P., Vho, A., Bovay, T., Airaghi, L., and Centrella, S.: Quantitative compositional mapping of mineral phases by
585 electron probe micro-analyser, *Geol. Soc. Spec. Publ.*, 478, 39-63, doi:10.1144/SP478.4, 2019.
- Lippard, S.J., Shelton, A.W., and Gass, I.G.: *The Ophiolite of Northern Oman*, Geological Society of London Memoir 11, Blackwell Scientific Publications, Oxford, 178 pp, 1986.
- Mayhew, L.E., Ellison, E.T., Miller, H.M., Kelemen, P.B., and Templeton, A.S.: Iron transformations during low temperature alteration of variably serpentinized rocks from the Samail ophiolite, Oman, *Geochim. Cosmochim. Acta*, 222, 704-728,
590 doi:10.1016/j.gca.2017.11.023, 2018.
- Matter, J.M., and Kelemen, P.B.: Permanent storage of carbon dioxide in geological reservoirs by mineral carbonation, *Nature Geosci.*, 2, 837-841, doi:10.1038/ngeo683, 2009.
- Menzel, M.D., Garrido, C.J., Sánchez-Vizcaíno V.L., Marchesi, C., Hidas, K., Escayola, M.P., and Huertas, A.D.: Carbonation of mantle peridotite by CO₂-rich fluids: the formation of listvenites in the Advocate ophiolite complex (Newfoundland,
595 Canada), *Lithos*, 323, 238-261, doi: 10.1016/j.lithos.2018.06.001, 2018.
- Menzel, M.D., Urai, J.L., de Obeso, J.C., Kotowski, A., Manning, C.E., Kelemen, P.B., Kettermann, M., Jesus, A.P., Harigane, Y., and the Oman Drilling Project Phase 1 Science Party: Brittle Deformation of Carbonated Peridotite-Insights From Listvenites of the Samail Ophiolite (Oman Drilling Project Hole BT1B), *J. Geophys. Res. Solid Earth*, 125, e2020JB020199, doi:10.1029/2020JB020199, 2020.
- 600 Menzel, M., Urai, J.L., Ukar, E., Schwedt, A., Hirth, G., Kovács, A., Kibkalo, L., and Kelemen, P.B.: Ductile deformation during carbonation of serpentinized peridotite, *EarthArXiv* [preprint], doi:10.31223/X53K87, 01 June 2021.
- Menzel, M., Urai, J.L., Ukar, E., Decrausaz, T., and Godard, M.: Evolution of vein microstructures during peridotite carbonation: insights from listvenites in Hole BT1B, Samail ophiolite (Oman), *Solid Earth Discuss.*, doi: 10.5194/se-2021-152, 2022.

- 605 Nasir, S., Al Sayigh, A.R., Al Harthy, A., Al-Khribash, S., Al-Jaaidi, O., Musllam, A., Al-Mishwat, A., and Al-Bu'saidi, S.: Mineralogical and geochemical characterization of listwaenite from the Semail Ophiolite, Oman, *Geochemistry*, 67, 213-228, doi:10.1016/j.chemer.2005.01.003, 2007.
- Nicolas, A., Boudier, F., Ildefonse, I., and Ball, E.: Accretion of Oman and United Arab Emirates ophiolite – Discussion of a new structural map, *Mar. Geophys. Res.*, 21, 147-180, doi:10.1023/A:1026769727917, 2000.
- 610 Noël, J., Godard, M., Oliot, E., Martinez, I., Williams, M., Boudier, F., Rodriguez, O., Chaduteau, C., Escario, S., and Gouze, P.: Evidence of polygenetic carbon trapping in the Oman Ophiolite: Petro-structural, geochemical, and carbon and oxygen isotope study of the Wadi Dima harzburgite-hosted carbonates (Wadi Tayin massif, Sultanate of Oman), *Lithos*, 323, 218-237, doi:10.1016/j.lithos.2018.08.020, 2018.
- Padrón-Navarta, J.A., López Sánchez-Vizcaíno, V., Hermann, J., Connolly, J.A.D., Garrido, C.J., Gómez-Pugnaire, M.T., and Marchesi, C.: Tschermak's substitution in antigorite and consequences for phase relations and water liberation in high-grade serpentinites, *Lithos*, 178, 186-196, doi:10.1016/j.lithos.2013.02.001, 2013.
- 615 Pitzer, K.S., and Sterner, S.M.: Equations of state valid continuously from zero to extreme pressures with H₂O and CO₂ as examples, *Int. J. Thermophys.*, 16, 511-518, doi:10.1007/BF01441917, 1995.
- Okazaki, K., Michibayashi, K., Hatakeyama, K., Abe, N., Johnson, K.T.M., and Kelemen, P.B., & the Oman Drilling Project Science Team: Major mineral fraction and physical properties of carbonated peridotite (listvenite) from ICDP Oman Drilling Project Hole BT1B inferred from X-ray CT core images, *J. Geophys. Res. Solid Earth*, 126, e2021JB022719, doi:10.1029/2021JB022719, 2021.
- 620 Power, I.M., Wilson, S.A., and Dipple, G.: Serpentinite Carbonation for CO₂ Sequestration, *Elements*, 9(2), 115-121, doi:10.2113/gselements.9.2.115, 2013.
- 625 Prigent, C., Agard, P., Guillot, S., Godard, M., and Dubacq, B.: Mantle wedge (de)formation during subduction infancy: evidence from the base of the Semail ophiolitic mantle, *J. Petrol.*, 59, 2061-2091, doi:10.1093/petrology/egy2090, 2018.
- Qiu, T., and Zhu, Y.: Listwaenite in the Sartohay ophiolitic mélange (Xinjiang, China): A genetic model based on petrology, U-Pb chronology and trace element geochemistry, *Lithos*, 302-303, 427-446, doi:10.1016/j.lithos.2018.01.029, 2018.
- Rious, M., Garber, J.M., Searle, M., Kelemen, P.B., Miyashita, S., Adachi, Y., and Bowring, S.: High-Precision U-Pb Zircon Dating of Late Magmatism in the Samail Ophiolite: A Record of Subduction Initiation, *J. Geophys. Res. Solid Earth*, 126, e2020JB020758, doi:10.1029/2020JB020760, 2021.
- 630 Scambelluri, M., Bebout, G.E., Belmonte, D., Gilio, M., Campomenosi, N., Collins, N., and Crispini, L.: Carbonation of subduction-zone serpentinite (high-pressure ophicarbonates; Ligurian Western Alps) and implications for the deep carbon cycling, *Earth Planet. Sci. Lett.*, 441, 155-166, doi:10.1016/j.epsl.2016.02.034, 2016.
- 635 Schwarzenbach, E.M., Früh-Green, G.L., Bernasconi, S.M., Alt, J.C., and Plas, A.: Serpentinization and carbon sequestration: A study of two ancient peridotite-hosted hydrothermal systems, *Chem. Geol.*, 351, 115-133, doi:10.1016/j.chemgeo.2013.05.016, 2013.

- Searle, M.J., and Cox, J.: Tectonic setting, origin, and obduction of the Oman ophiolite, *Geol. Soc. Am. Bull.*, 111, 104-122, doi:10.1130/0016-7606(1999)111<0104:TSOAOO>2.3.CO;2, 1999.
- 640 Seifritz, W.: CO₂ disposal by means of silicates, *Nature*, 345, 486
- Sofiya, A., Ishiwatari, A., Hirano, N., and Tsujimori, T.: Relict chromian spinels in Tulu Dimtu serpentinites and listvenite, Western Ethiopia: implications for the timing of listvenite formation, *Int. Geol. Rev.*, 59, 1621-1631, doi: 10.1080/00206814.2016.1213142, 2017.
- Soret, M, Agard, P, Dubacq, B, Plunder, A, and Yamato, P.: Petrological evidence for stepwise accretion of metamorphic soles during subduction infancy (Semail ophiolite, Oman and UAE), *J. Metamorph. Geol.*; 35(9), 1051-1080, doi:10.1111/jmg.12267, 2017.
- 645 Stanger, G.: Silicified serpentinite in the Semail nappe of Oman, *Lithos*, 18, 13-22, doi:10.1016/0024-4937(85)90003-9, 1985.
- Takazawa, E., Okayasu, T., and Satoh, K.: Geochemistry and origin of the basal lherzolites from the northern Oman ophiolite (northern Fizh block), *Geochem. Geophys.*, 4(2), 1021, doi:10.1029/2001GC000232, 2013.
- 650 Tominaga, M., Beinlich, A., Lima, E.A., Tivey, M.A., Hampton, B.A., Weiss, B., and Harigane, Y.: Multi-scale magnetic mapping of serpentinite carbonation, *Nat. Commun.*, 8, 1870, doi:10.1038/s41467-017-01610-4, 2017.
- Ulrich, M., Muñoz, M., Guillot, S., Cathelineau, M., Picard, C., Quesnel, B., Boulvais, P., and Couteau, C.: Dissolution-precipitation processes governing the carbonation and silicification of the serpentinite sole of the New Caledonia ophiolite. *Contrib. Mineral. Petrol.*, 167, 952, doi:10.1007/s00410-013-0952-8, 2014.
- 655 Villey, M., Le Metour, J., and De Gramont, X.: Geological map of Fanja, Sheet NF 40-3F. Explanatory Notes, BRGM and Oman Ministry of Petroleum & Minerals, 1986.
- Wilde, A., Simpson, L., and Hanna, S., Preliminary study of Cenozoic hydrothermal alteration and platinum deposition in the Oman Ophiolite, *J. Virtual Explor.*, 6, 7-13, 2002.

This manuscript submitted to EarthArXiv is a preprint that has not undergone full peer review yet. It has been submitted to and is under consideration in the European Journal of Mineralogy. If accepted there, the final version will be available via the peer-reviewed publication DOI. Please feel free to contact the authors, we welcome any feedbacks.

Pervasive carbonation of peridotite to listvenite (Semail Ophiolite, Sultanate of Oman): clues from iron partitioning and chemical zoning

Supporting Information

Thierry Decrausaz¹, Marguerite Godard¹, Manuel Menzel^{2,3}, Fleurice Parat¹, Emilien Olliot¹, Romain Lafay¹, Fabrice Barou¹

¹Géosciences Montpellier, University of Montpellier, CNRS, Montpellier, 34095, France

²Tectonics and Geodynamics, RWTH Aachen University, Aachen, D-52056, Germany

³Instituto Andaluz de Ciencias de la Tierra (IACT), CSIC-UGR, Armilla, 18100, Spain

Contents of this file

Text S1

Figures S1 to S5

Captions for Figures S1 to S5

Additional Supporting Information (Files uploaded separately)

Captions for Tables S1 to S11

Introduction

Supporting Information files comprise detailed geological maps, cross-sections, field photographs of the investigated areas (Fig. S1), in complement to field observations (Text S1-1), and information on lithological columns and sampling presented in Fig. 1. Location, rock types, mineralogy and microstructures of studied samples are reported in Tables S1 and S2. A detailed

description of the analytical techniques used to acquire the geochemical dataset presented in this article (Tables S3-S11) is provided in Text S1-2.

1 Geological setting: field observations, mapping, and sampling along Wadi Mansah (OmanDP Hole BT1B, Site 1) and the Jebel Fanja (Site 2)

In the Fanja region (23.465760°N, 58.108835°E), listvenites crop out along NW-SE direction, interlayering ophiolite mantle segments atop the metamorphic sole and autochthonous sediments of the Arabian margin on the flanks of the Jebel Akhdar and Saih Hataf domes (Fig. 1b). Listvenites extend at the kilometre-scale forming the ridges of the Jebel Fanja and the Jebel Qarn westwards, while coinciding with a broad anticline (MoD mountain) along Wadi Mansah (Kelemen et al., 2022). Listvenites occur as layers or lenses within serpentinized peridotites, oriented parallel to the ophiolite basal thrust. Sharp reaction fronts from listvenites to carbonated serpentinites (ca. 5-30 m) and serpentinized peridotites (harzburgites when not fully serpentinized) are observed. Serpentinized peridotites, carbonated serpentinites and listvenites were collected at 3 locations (Fig. 1b): Oman Drilling Project Hole BT1B (23.364374°N, 58.182693°E) and Site 1 (23.346010°N, 58.221083°E) in Wadi Mansah, and Site 2 (23.448299°N, 58.201763°E) in the Jebel Fanja. At Hole BT1B location, a continuous section including the base of the ophiolite mantle atop the basal thrust and underlying metamorphic sole was drilled (Kelemen et al., 2020). Similar approach was adopted for fieldwork at Site 1 and Site 2 by investigating transects from the top of the metamorphic sole, through the mantle section, up to overlying lower crustal gabbros. Detailed geological maps, cross-sections, constructed lithological columns, and field photographs for Site 1 and Site 2 are provided in Fig. S1. Maps and cross-sections were drawn after Villey et al. (1986) and Kelemen et al. (2022), and adjusted based on field studies. The topography was drawn after Google Earth topographic map. Lithological columns were constructed after cross-sections and field observations. In the same way as Hole BT1B, thicknesses of layers were considered perpendicularly to the contact atop the sole.

Hole BT1B was drilled in the north-western part of Wadi Mansah, on the southern flank of the MoD mountain (Fig. 1b). The ophiolite mantle (thickness not known, but most likely >150 m; Kelemen et al., 2022) is made of interlayered serpentinized peridotites (harzburgites and minor dunites), carbonated serpentinites and listvenites. It overlies >100 m of metamorphosed rocks consisting of mafic-derived material (pillow metabasalts, amphibolites) and metasediments (mainly radiolarites). All layers gently dip to the South at surface as presented in Kelemen et al. (2022) and confirmed by fieldwork (e.g., contact listvenite–carbonated serpentinite: 138/20, GPS: 23°22'05.1"N, 58°11'06.9"E). As layers are verticalized at depth, Hole BT1B was drilled with an inclination of 75° with respect to the horizontal ground to ensure drilling through the mantle section and the metamorphic sole (Kelemen et al., 2020). The recovered core section included ~197 m of listvenites and fuchsite-bearing listvenites layered by two intervals of carbonated serpentinites (80.28-100.23 and 181.26-185.47 meters below ground – m.b.g.), atop of >100 m of metabasalts (Fig 1c; Kelemen et al., 2020; Godard et al., 2021). The geochemical study of carbonated serpentinites and listvenites revealed similarities with the “Banded Unit” peridotites: in details, 3 chemically distinct domains derived from various protoliths (alternating harzburgites/dunites and lherzolites) were identified (Fig 1c; Godard et al., 2021). Fuchsite-bearing listvenites are essentially comprised within the domain derived from a lherzolitic protolith (Godard et al., 2021). Selected samples for this study comprise 15 listvenites, 5 fuchsite-bearing listvenite, and 8 carbonated serpentinites to encompass the entire drilled mantle section and all domains.

Site 1 is located in the south-eastern part of Wadi Mansah (Fig. 1b, Fig. S1). In contrast to the drilled sequence (Hole BT1B), the mantle section here is thicker (>250 m) and is composed principally of massive, slightly serpentinized harzburgites and rare dunites. The underlying metamorphic sole comprises a sequence including, from top to bottom, mafic-derived rocks, radiolarites and shales. Listvenites on the field show a typical stain orange-red weathering colour and are found (i) atop the metamorphic sole to the North, where they form a discontinuous thin layer (~2-10 m) in contact with the main basal thrust, and below ~20 m of foliated and fractured carbonated serpentinites (Fig. S1); and (ii) interlayered in carbonated serpentinites close to the faulted mantle–gabbros contact to the South (Figures 1c and S1). All these lithological boundaries dip to the South (contact metamorphic sole–listvenites: 178/57, GPS: 23.357223°N, 58.219827°E; contact listvenites–carbonated serpentinites: 188/46; GPS: 23.345901°N, 58.221218°E). In the southern part, listvenites form a 10-50 m thick interlayer bordered by foliated and fractured carbonated serpentinites, 5-10 m away from the faulted contact with foliated gabbros. Stain orange-red listvenites host discontinuous millimetric to centimetric white quartz-carbonate veins oriented at high angle with the lithological contact. Fault contacts between listvenites, serpentinites and gabbro are highly variable, ranging from serpentinites fault gouge to foliated serpentinites, with sharp localized faults. Close to gabbros, carbonated serpentinites host scarce gabbroic dikelets (<10 cm thick) or pods. Below listvenites, ~25-50 m of foliated serpentinites show extensive matrix replacement by carbonates. Collected samples in Site 1 encompass the mantle-metamorphic sole transition (n=2; OM20-11 and OM20-12, Fig. S1), the main harzburgitic section (n=1; OM20-13), and the upper transition between carbonated serpentinites and listvenites (n=5; OM20-14, OM20-15, OM20-16, OM20-17, OM20-18) (Fig 1c, Table S1).

Site 2 is located in the north-eastern part of the Jebel Fanja (Fig. 1b-c, Fig. S1). This area is characterized by a mantle section 150-200 m) made of often foliated and fractured serpentinized harzburgites (~100 m thick), interlayered by bands of listvenites close to overlying lower crustal gabbros. Serpentinized harzburgites (~100 m thick) overly the metamorphic sole comprising a sequence composed of, from top to bottom, mafic-derived schists and locally amphibolites along the basal thrust (GPS: 23.447692°N, 58.202856°E), shales and micaschists. In this studied site, all lithological boundaries dip to the NNW (contact serpentinized peridotites–metamorphic sole: 337/60; GPS: 23.446848°N, 58.203809°E; contact listvenite–carbonated serpentinite: 352/28, GPS: 23.448760°N, 58.202344°E). Two transects were investigated (cross-sections A-B and C-D). Listvenites occur as kilometre-scale continuous structural level draping the ridge and southern flank of Jebel Fanja (~50-75 m, Fig. 1b), and as plurimetric lenses bordered by carbonated serpentinites. Massive stain orange-red listvenites are cut by closely spaced sub-millimetric red carbonate veins and by pluri-millimetric white quartz-carbonate veins (Fig. S2), all being oriented perpendicular to the southern contact with underlying carbonated serpentinites (~3-20 m). Those latter are foliated close to listvenites (Fig. S2), hosting millimetric to centimetric light orange carbonate veins, oriented sub-parallel to the contact (Fig. S1). Vein density increases towards the serpentinites-listvenites contact. Few millimetric red carbonate veins cut through both listvenites and carbonated serpentinites. Listvenites to the North are overlain by deformed serpentinized peridotites (>20 m) crosscut by numerous gabbroic dikes and pods at proximity with gabbros. Sampling in Site 2 encompass the main section of serpentinized peridotites (n=1; OM20-28), the transition between carbonated serpentinites and listvenites (n=6; OM20-25,

OM20-26, OM20-29, OM30-30b, OM20-31, OM20-32) and serpentinized peridotites comprised between listvenites and gabbros (n=1; OM20-34) (Figs 1c, S1, Table S1).

2 Methods

The petrographic study was realized on 29 samples from Hole BT1B, and 16 samples from Site 1 (n=8) and Site 2 (n=8) mapped areas. A subset of 9 samples was analysed by scanning electron microscopy (SEM/EDS). 25 samples were analysed by electron probe micro-analysis (EPMA) and the composition of carbonates in transition metals was determined by laser ablation inductively-coupled plasma mass spectrometry (LA-ICP-MS) on 12 samples (Table S1).

2.1 Rock types, mineralogy and microstructures

The rock type, mineral assemblage, phase abundance, and microstructures were determined by the petrographic study of thin sections. Observations are summarized in Table S2.

The rock type was assigned after the assemblage of predominant matrix-forming minerals. Serpentinized peridotites are made of various proportions of serpentine and relic primary olivine, orthopyroxene, and clinopyroxene. Carbonated serpentinites are mainly composed of serpentine and Mg-carbonates (magnesite, dolomite), while listvenites are formed of quartz and Mg-carbonates (magnesite, dolomite), occasionally fuchsite-bearing. Cr-spinel and Fe-oxides are present in all samples. Sulfides are observed in most serpentinized peridotites and carbonated serpentinites, but are rare in listvenites.

Samples are generally massive, with high proportions of reacted host rock (matrix) with respect to veins (estimated at the core scale for BT1B samples; Kelemen et al., 2020). Low sum of host rock and vein proportions is related to the presence of cataclasites (Menzel et al., 2020). To indicate the type of deformation recorded by samples, the term “veined” is used for brittle deformation related to vein formation, while “foliated” and “cataclasite” are used for samples displaying shear-induced microstructures and cataclasites, respectively.

Identification of the carbonate phase, occurrence of Mg-core and Fe-core spheroids (described in the main text), and abundance of matrix and vein carbonates rely on microscopic observations, and confirmed by SEM/EDS imaging and/or in-situ quantification.

Carbonated serpentinites and listvenites host an intricate network of serpentine-bearing, carbonate-bearing and quartz-bearing veins, classified by Menzel et al. (2022) after the vein mineralogy, morphology, growth habit, and cross-cutting relationships. Vein types and their abundancy are reported in Table S2. Vein nomenclature is constructed as follows: a) the first letter indicate the host rock (“s” for serpentinized peridotite and carbonated serpentinite; “l” for listvenite); b) the second letter refers to the main filling mineral (“s” for serpentine, “c” for carbonate, “q” for quartz); c) the number indicate the timing of vein formation based on cross-cutting relationships. In this study, we focussed on early carbonate veins common in carbonated serpentinites

(sc0, sc2) and listvenites (lss0, lss2, lc1, lc2). Thus, late carbonate-bearing and quartz-bearing veins (sc3 to sc4 and lc3 to lc6 subtypes) are not described in the main text. The sq1 set corresponds to feathery quartz veins (<50 μm). Syntaxial lq4 veins (< 250 μm) are made of chalcedony borders and tabular magnesite in the median zone. Syntaxial lc4 veins (> 1 mm) are made of dolomite and quartz showing euhedral growth facets. Syntaxial sc4 and lc6 veins (0.1-5 mm) are the latest ones, crosscutting all previously formed structures, and are made of euhedral dolomite.

2.2 Mineral identification and chemistry

2.2.1 EDS

Energy-dispersive X-ray spectroscopy (EDS) maps were acquired on polished thin sections using a CamScan CrystalProbe X500FE instrument, equipped with an UltimMax 100 EDS detector at the Géosciences Montpellier SEM-EBSD facility (University of Montpellier). Mapping was performed under low vacuum (2 Pa) on tilted samples (70° inclination), at a working distance of 25 mm, and an acceleration voltage of 20 kV. The step size was 1.2 μm , except for the high resolution imaging of the cryptocrystalline quartz matrix, and of zoning within spheroids (0.7 μm).

2.2.2 EPMA quantification and mapping

The major element compositions of carbonates, silicates (serpentine, fuchsite), oxides and sulfides were quantified using a Cameca SX100 (Géosciences Montpellier) and a JEOL JXA-8530F HyperProbe (ISTE, University of Lausanne, Switzerland) electron microprobe. Operating conditions for silicates were an acceleration voltage of 15 kV, a probe current of 10 nA at Géosciences Montpellier and of 15 nA at ISTE, and a widened beam (10 μm) to prevent damage/devolatilization of the analysed phase. Carbonates were analysed in similar conditions except for a reduced beam size (3, 5 or 10 μm). For oxides and sulfides, the probe current was increased to 20 nA and the beam was focussed. It was eventually increased to 2 μm to measure large, homogeneous Cr-spinel or Fe-oxide grains ensuring current stability. Elemental mapping was performed at ISTE, using an acceleration voltage of 15 kV, a probe current of 20 nA, and a defocussed beam (2 μm). Step size was 1 μm and dwell times 100 ms. Quantification of elemental maps was achieved by computing X-ray intensities and in-situ chemistry data through XMapTools 3.4.1 MatLab toolbox (Lanari et al., 2014, 2019). Quantification of elemental maps was realized by computing X-ray intensities through XMapTools, with internal standardization based on punctual EPMA analyses.

Standard deviation and detection limits of each element are listed in Table S3 The compositions of carbonates, serpentines and fuchsite, Cr-spinel, Fe-oxides and sulfides are given in Tables S4, S5, S6, S7, and S8, respectively.

It should be noted that several carbonate analyses indicate non negligible amounts of SiO_2 (>1 wt%). High SiO_2 content is not caused by beam displacement or overlapping of analysis spot with adjacent serpentine or quartz grains: it reflects the presence of nano-inclusions of silica within carbonates (serpentine in carbonated serpentinites, silica in listvenite), evidenced by STEM-HAADF imagery in Beinlich et al. (2020). Measured SiO_2 content values <1 wt% indicate measurement of a pure carbonate phase, while values >1 wt% are associated with the presence of serpentine/silica inclusions. In Fig. 4, only measurements with

SiO₂ content <1 wt% are plotted. In Fig S6, carbonate compositions are plotted in Mg+Ca-Si-Fe ternary diagrams to account for the presence of serpentine/silica inclusions within carbonates.

2.2.3 HR-LA-ICP-MS

Compositions of carbonates in transition metals (Sc, Ti, V, Mn, Fe, Co, Ni, Cu, Zn) were determined by HR-LA-ICP-MS over 4 sessions of measurements.

A first batch of analyses was performed at ISTE (University of Lausanne), using a ThermoScientific Element XR mass spectrometer interfaced to a New Wave ArF 193 nm laser. Spot diameter for analysis was 100 µm, with on-sample energy density of 7 J/cm² and a repetition rate of 12 Hz. Data were collected in time resolved acquisition mode, with 120 s dedicated to background signal measurement followed by 45 s of sample ablation. Instrument mass bias was calibrated by 16 measurements of NIST SRM 612 reference material (synthetic glass). Calibration was controlled by 6 measurements of BCR-2G reference material (basaltic glass).

Other batches of analysis were carried out at Géosciences Montpellier (AETE-ISO, OSU OREME), using a ThermoScientific Element 2 mass spectrometer coupled to an Excimer G2 193 nm laser. Spot diameter for analysis was 110 µm (pre-ablated at 130 µm), with on-sample energy density of 6 J/cm² and a repetition rate of 7 Hz, to avoid contamination of neighbouring crystal grains to the ablation spot. Data were collected in time resolved acquisition mode, with 120 s dedicated to background signal measurement followed by 40 s of sample ablation. Instrument mass bias was calibrated by 24 measurements of NIST SRM 612 reference material. Calibration was controlled by 17 measurements of BIR-1G reference material (basaltic glass).

Raw data were processed using the data reduction software Glitter (Griffin et al., 2008), using the linear fit to ratio method. CaO content obtained by EPMA analysis was used as internal standard for quantification. Table S9 Values obtained for certified rock materials NIST SRM 612, BIR-1G and BCR-2G are given in. Trace elements compositions of carbonates are provided in Table S10. Compiled transition metals compositions of carbonates are given as median compositions, and 16th and 84th percentiles in Table S11.

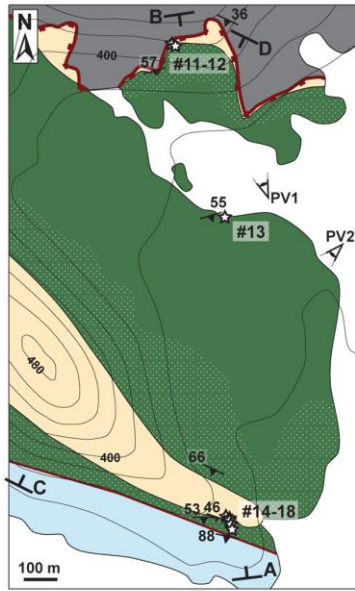
References

Beinlich, A., Plümper, O., Boter, E., Müller, I. A., Kourim, F., Ziegler, M., Harigane, Y., Lafay, R., Kelemen, P.B., the Oman Drilling Project Science Team: Ultramafic rock carbonation: Constraints from listvenite core BT1B, Oman drilling project, *J. Geophys. Res. Solid Earth*, 125, e2019JB019060, doi:10.1029/2019JB019060, 2020.

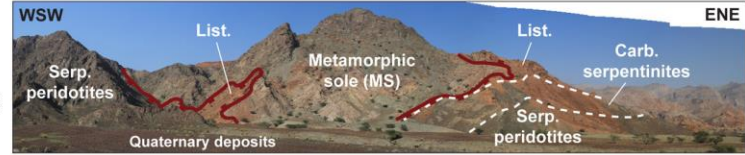
Godard, M., Carter, E.J., Decrausaz, T., Lafay, R., Bennett, E., Kourim, F., de Obeso, J.C., Michibayashi, K., Harris, M., Coggon, J., Teagle, D., Kelemen, P., the Oman Drilling Project Phase 1 Science Party.: Geochemical Profiles Across the

- Listvenite-Metamorphic Transition in the Basal Megathrust of the Semail Ophiolite: Results from Drilling at Oman DP Hole BT1B, *J. Geophys. Res. Solid Earth*, 126, e2021JB022733, doi:10.1029/2021JB022733, 2021.
- Griffin, W., Powell, W., Pearson, N.J., O'Reilly, S.: GLITTER: data reduction software for laser ablation ICP-MS, *Short Course Series*, 40, 308-311, 2008.
- Kelemen, P.B., Matter, J.M., Teagle, D.A.H., Coggon, J.A., and the Oman Drilling Project Science Team: Site BT1: fluid and mass exchange on a subduction zone plate boundary, in: *Proceedings of the Oman Drilling Project*, College Station, Texas (International Ocean Discovery Program), doi:10.14379/OmanDP.proc.2020, 2020.
- Kelemen, P.B., de Obeso, J.C., Leong, J.A., Godard, M., Okazaki, K., Kotowski, A.J., Manning, C.E., Ellison, E.T., Menzel, M.D., Urai, J.L., Hirth, G., Rioux, M., Stockli, D.F., Lafay, R., Beinlich, A.M., Coggon, J.A., Warsi, N.H., Matter, J.M., Teagle, D.A.H., Harris, M., Michibayashi, K., Takazawa, E., Al Sulaimani, Z. and the Oman Drilling Project Science Team: Listvenite formation during mass transfer into the leading edge of the mantle wedge: Initial results from Oman Drilling Project Hole BT1B, *J. Geophys. Res. Solid Earth*, 127, e2021JB022352, doi:10.1029/2021JB022352, 2022.
- Lanari, P., Vidal, O., De Andrade, V., Dubacq, B., Lewin, E., Grosch, E., Schwartz, S.: XMapTools: a MATLAB©-based program for electron microprobe X-ray image processing and geothermobarometry, *Computers and Geosciences*, 62, 227-240, doi:10.1016/j.cageo.2013.08.010, 2014.
- Lanari, P., Vho, A., Bovay, T., Airaghi, L., Centrella, S.: Quantitative compositional mapping of mineral phases by electron probe micro-analyser, *Geological Society, London, Special Publications*, 478, 39-63, doi:10.1144/SP478.4, 2019.
- Menzel, M.D., Urai, J.L., de Obeso, J.C., Kotowski, A., Manning, C.E., Kelemen, P.B., Kettermann, M., Jesus, A.P., Harigane, Y., and the Oman Drilling Project Phase 1 Science Party: Brittle Deformation of Carbonated Peridotite-Insights From Listvenites of the Semail Ophiolite (Oman Drilling Project Hole BT1B), *J. Geophys. Res. Solid Earth*, 125, e2020JB020199, doi:10.1029/2020JB020199, 2020.
- Menzel, M., Urai, J.L., Ukar, E., Schwedt, A., Hirth, G., Kovács, A., Kibkalo, L., and Kelemen, P.B.: Ductile deformation during carbonation of serpentinized peridotite, *EarthArXiv* [preprint], doi:10.31223/X53K87, 01 June 2021.
- Villey, M., Le Metour, J., De Gramont, X.: Geological map of Fanja, Sheet NF 40-3F. Explanatory Notes, BRGM and Oman Ministry of Petroleum & Minerals, 1986.

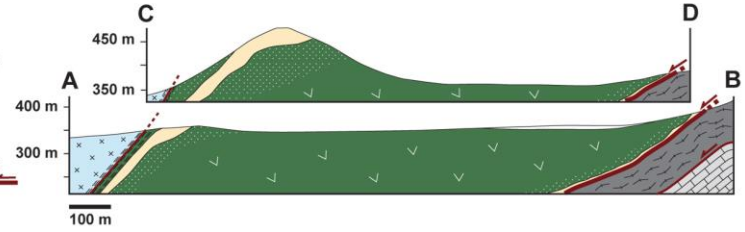
Site 1: Wadi Mansah



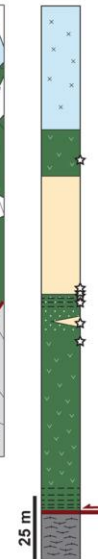
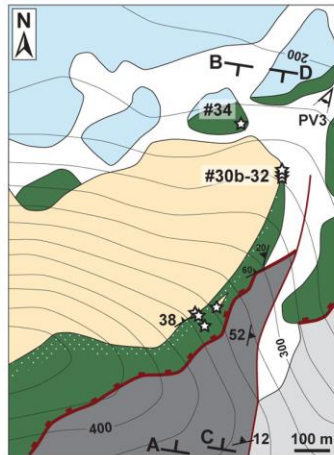
Panoramic view 1



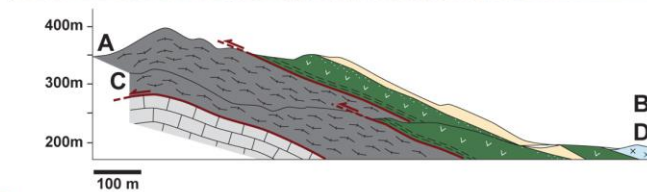
Panoramic view 2



Site 2: Jebel Fanja



Panoramic view 3



Lithologies		Structural marks			
Semail Ophiolite		Gabbro		Major thrust (today in normal fault position)	
		Listvenite		Fault	
		Carbonated serpentinite		55	Lithological contact
		Serpentinized peridotite		12	Foliation plane and dip
		Metamorphic sole			Foliation (only for cross-sections and logs)
		Hawasina metasediments			

Figure S1: Detailed geological maps, lithological columns, cross-sections and field photographs for Site 1 (Wadi Mansah) and Site 2 (Jebel Fanja). Detailed maps were drawn after Villey et al. (1986) and field observations (this study, see Text S1-1). The topography was drawn from Google Earth maps. Location of samples is indicated by white stars; adjacent numbers refers to sample names. Lithological columns were constructed from cross-sections. The thickness of lithological layers was calculated perpendicular to the metamorphic sole. Field photographs illustrate panoramas of investigated transects.

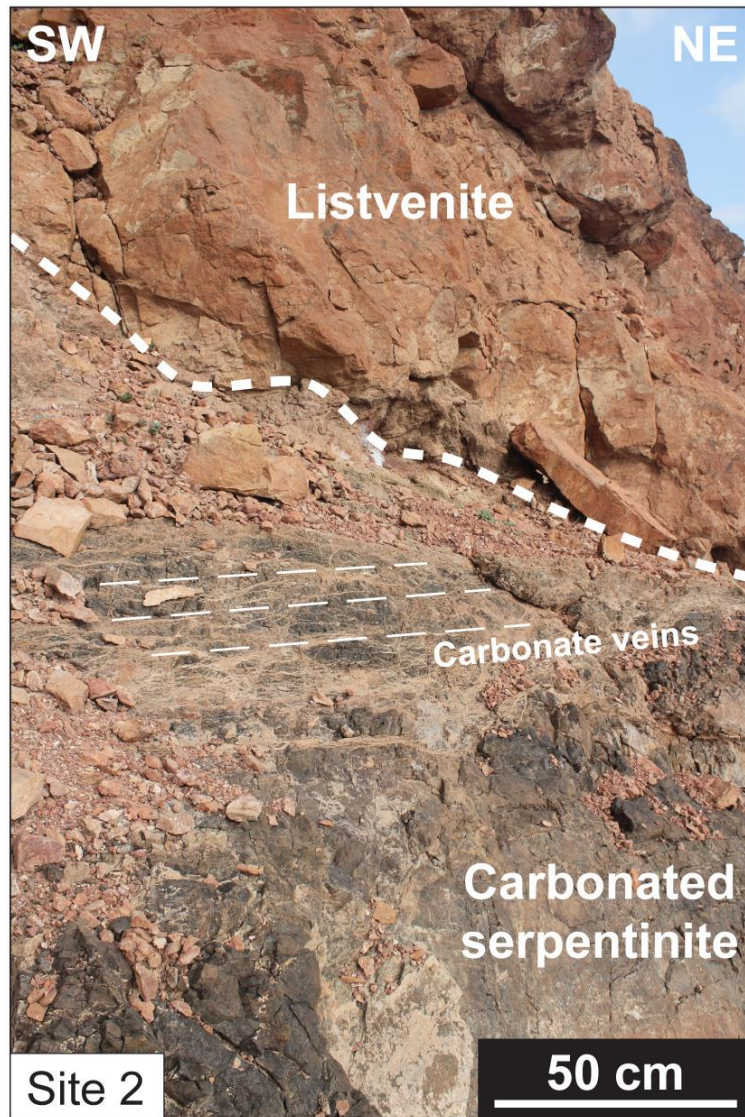


Figure S2: Field photographs at the Site 2 illustrating the transition from foliated carbonated serpentinites to massive listvenites (Site 1 and Site 2). Carbonated serpentinites host magnesite veins oriented at low angle to the contact (Site 2), with vein density increasing towards the contact with listvenites.

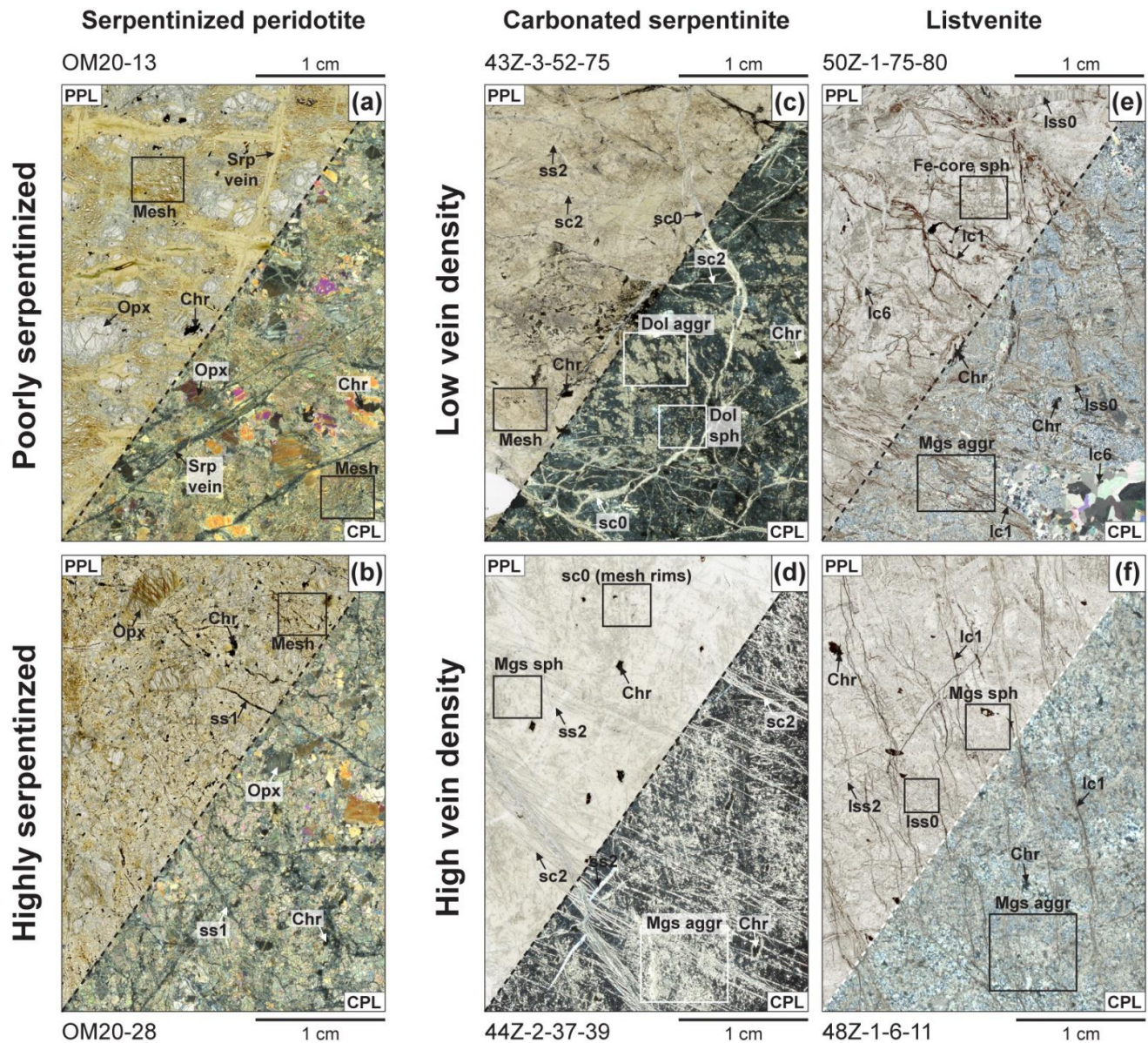


Figure. S3: Plane-polarized light (PPL) and crossed-polarized light (CPL) thin section photographs of representative samples of serpentinitized harzburgites (a, b), and of variously veined carbonated serpentinites (c, d) and listvenites (e, f) from the Fanja area. Moderately serpentinized harzburgites (a) are porphyroclastic with subcentimetric fractured orthopyroxene (noted Opx), Cr-spinels (noted Chr) and mesh texture serpentine formed after olivine (noted Mesh), and are crosscut by millimetre-thick light greenish-yellowish serpentine veins (noted Srp vein). Highly serpentinized harzburgites (b) are distinguished by high amounts of magnetite (black strings in mesh) and abundant fine magnetite-rich serpentine veins (noted ss1). Carbonated serpentinites are made of a fine-grained matrix of serpentine and carbonates, cut by diverse serpentine crack-seal veins (noted

ss2), pseudomorphic carbonate after serpentine veins (noted sc0) and early antitaxial carbonate veins (noted sc2). Listvenites display a fine-grained matrix of quartz and carbonates, cut by diverse pseudomorphic carbonate after serpentine mesh rims (noted lss0) and crack-seal veins (noted lss2), by early antitaxial magnesite veins (noted lc1) and late dolomite veins (noted lc6). Matrix carbonates occur as aggregates (noted aggr) or isolated grains (sph). Location of Mg-rich and Fe-rich core magnesite spheroids, and aggregates are indicated by white/black rectangles (see main text for further information). Vein terminology after Menzel et al. (2022). Abbreviation: Dol: dolomite; Mgs: magnesite, Srp: serpentine.

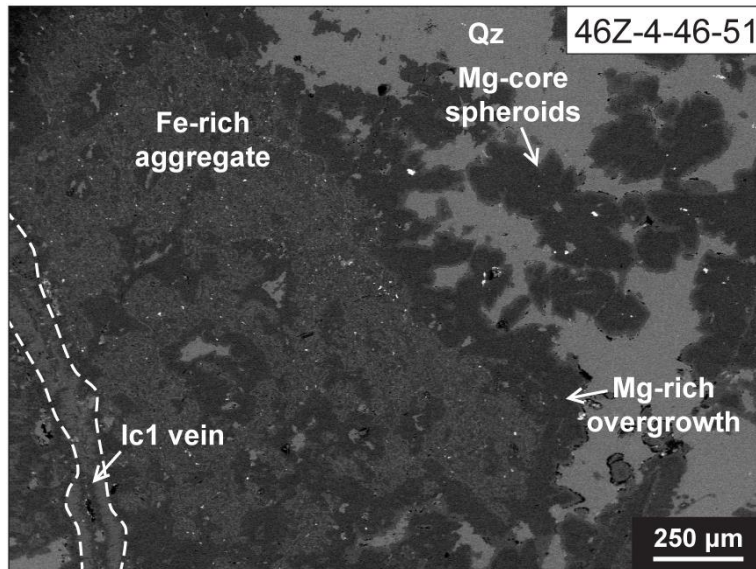


Figure. S4: Back-scattered electron (BSE) image of Fe-rich magnesite (light grey) clustering in the vicinity of early carbonate veins (noted lc1), and overgrown by Mg-rich magnesite (dark grey) in listvenite 46Z-4-46-51. Magnesite spheroids away from the vein are also Mg-rich. Abbreviation: Mgs: magnesite; Qz: quartz.

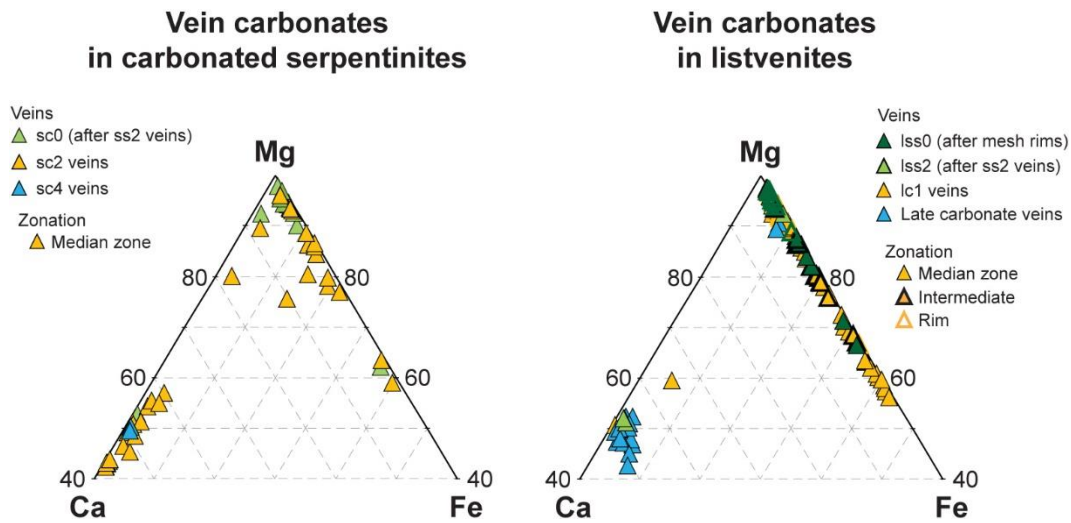


Figure. S5: Major element compositions of vein carbonates in carbonated serpentinites and listvenites, represented in Mg-Ca-Fe ternary diagrams. The proportions of each end-member was calculated from EPMA compositions as the cationic fraction of $M^{2+}/(Fe+Mg+Ca)$ ($M^{2+} = Fe, Mg$ or Ca). Analysed area is indicated for chemically zoned carbonates (median zone, intermediate, rim). Vein terminology after Menzel et al. (2022). Abbreviations: Dol: dolomite; Mgs: magnesite.

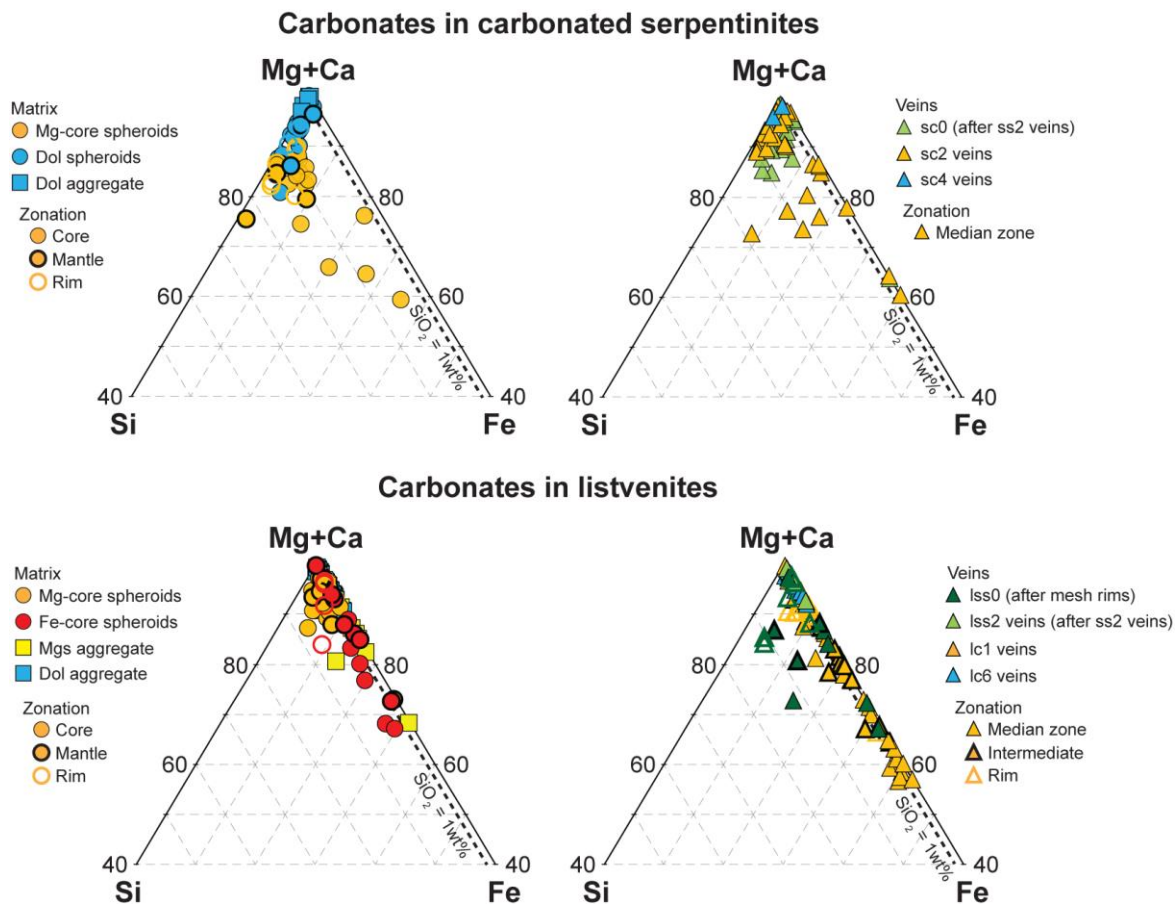


Figure. S6: Major element compositions of matrix and vein carbonates in carbonated serpentinites and listvenites, represented in Mg+Ca-Si-Fe ternary diagrams. The proportions of each end-member was calculated from EPMA compositions as the cationic fraction of $M/(Fe+Mg+Ca+Si)$ ($M = Fe, Mg+Ca$ or Si). Mg was associated to Ca to highlight the presence of serpentine and silica nano-inclusions with the crystal lattice of carbonates. Analysed area is indicated for chemically zoned carbonates (core, intermediate, rim). Vein terminology after Menzel et al. (2022). Abbreviations: Dol: dolomite; Mgs: magnesite.

Table captions:

Table S1 List of rock samples and applied analytical techniques. Full ICDP sample names are given for OmanDP Hole BT1B core samples. Location of samples is provided in the WGS84 coordinate system. Depth of core samples is in metres below the ground (m.b.g.). Distance to the metamorphic sole was calculated for BT1B samples and extrapolated from cross-sections and field observations for Site 1 and Site 2 samples (see Text S1). BT1B core geochemical domains were determined by Godard et al. (2021). Both matrix and vein carbonates and serpentine were analysed by EPMA for in-situ quantification. Abbreviations for techniques: EBSD: electron backscatter diffraction; EDS: energy dispersive X-ray spectroscopy; EPMA: electron probe micro-analysis; LA-ICP-MS: laser ablation inductively coupled plasma mass spectrometry. Abbreviations for minerals: Carb: carbonates; Chr: chromite; Fu: fuchsite; Hem: hematite, Mlr: millerite; Py: pyrite; Srp: serpentine.

Table S2 Mineralogy and microstructures of rock samples. The mineral assemblage and phase abundance were determined optically. Magnesite and dolomite proportions in matrix and veins (noted (-) or (+)), and identification of Mg-core and Fe-core spheroids, rely on the thin-section study and SEM imaging. Vein types were determined after the vein classification by Menzel et al. (2022). Host rock and vein proportions of BT1B samples are reported from Kelemen et al. (2020), and optically estimated for Site1 and Site 2 samples. Low sum of host rock and vein proportions is related to the presence of cataclasites. To indicate the type of deformation recorded by samples, the term “veined” is used for brittle deformation and vein formation, while “foliated” and “cataclasite” are used for samples showing shear-derived structures or cataclasites, respectively. Abbreviations: m.b.g.: metres below ground, M: major; m: minor; t: trace. Abbreviations for minerals: Dol: dolomite; Mgs: magnesite.

Table S3 Average standard deviation and detection limits for EPMA analyses

Table S4 Major element compositions of carbonates determined by EPMA. Cations were recalculated on 6O per formula unit. Site ratios were calculated as the cationic fraction of $M^{2+}/(Fe+Mg+Ca)$ (i.e. $X_{Fe} = Fe/(Fe+Mg+Ca)$). Analysed area (median zone-intermediate-rim for vein carbonates, core-mantle-rim for matrix carbonates) is indicated for zoned carbonate. Vein nomenclature was adopted from Menzel et al. (2022). Abbreviations: bdl: beyond detection limit; m.b.g.: metres below ground; n.a.: not analysed; n.d.: not determined; GM: Géosciences Montpellier; ISTE: Institute of Earth Sciences.

Table S5 Major element compositions of serpentine and fuchsite determined by EPMA. Cations were recalculated on 7O per formula unit for serpentine and 22O per formula unit for fuchsite. Vein nomenclature was adopted from Menzel et al. (2022). Abbreviations: bdl: beyond detection limit; m.b.g.: metres below ground; n.a.: not analysed; n.d.: not determined; GM: Géosciences Montpellier; ISTE: Institute of Earth Sciences.

Table S6 Major element compositions of Cr-spinel determined by EPMA. Cations were recalculated on 4O per formula unit. Mg# and Cr# were calculated as cationic fractions: $Mg\# = (Mg/(Mg+Fe))$ and $Cr\# = (Cr/(Cr+Al))$. Abbreviations: bdl: beyond

detection limit; m.b.g.: metres below ground; n.a.: not analysed; n.d.: not determined; GM: Géosciences Montpellier; ISTE: Institute of Earth Sciences.

Table S7 Major element compositions of Fe-oxides determined by EPMA. Cations were recalculated on 3O per formula unit.. Abbreviations: bdl: beyond detection limit; m.b.g.: metres below ground; n.a.: not analysed; n.d.: not determined; GM: Géosciences Montpellier

Table S8 Major element compositions of sulphides determined by EPMA. Abbreviations: bdl: beyond detection limit; m.b.g.: metres below ground; GM: Géosciences Montpellier

Table S9 Trace element concentrations and preferred values of certified rock standards NIST-612, BIR-1G, BCR-2G determined by LA-ICP-MS. Preferred values from a compilation of literature values downloaded over the 2020-2022 period from the GeoReM database (<http://georem.mpch-mainz.gwdg.de>). Vein nomenclature was adopted from Menzel et al. (2022). Abbreviations: n.a.: not analysed.

Table S10 Compositions in transition metals determined by LA-ICP-MS. EPMA CaO content used for signal data reduction on Glitter is indicated. Concentrations are in $\mu\text{g/g}$, except for Fe (wt%). Vein nomenclature was adopted from Menzel et al. (2022). BT1B core geochemical domains after Godard et al., 2021. Abbreviations: bdl: beyond detection limit; m.b.g.: metres below ground; n.a.: not analysed; n.d.: not determined; GM: Géosciences Montpellier; ISTE: Institute of Earth Sciences.

Table S11 Compiled transition metals compositions of carbonates in carbonated serpentinite, listevnite, fuchsite-bearing listvenite. Median compositions, and 16th and 84th percentiles are provided. Concentrations are in $\mu\text{g/g}$, except for Fe (wt%). The Cr content and Fe/Mn ratio are derived from EPMA data. Vein nomenclature was adopted from Menzel et al. (2022). Abbreviations: n.a.: not analysed, n.d.: not determined.